

Unterschrift des Betreuers



TECHNISCHE  
UNIVERSITÄT  
WIEN  
Vienna University of Technology



## Diplomarbeit

# EROSION OF TUNGSTEN SURFACES BY NITROGEN IONS

Ausgeführt am Institut für  
Angewandte Physik  
der Technischen Universität Wien  
Wiedner Hauptstraße 8-10 / 134  
1040 Wien

unter der Anleitung von  
Proj. Ass. DI Katharina DOBES  
und  
Univ.-Prof. Dr. Friedrich AUMAYR

durch  
**Paulus NADERER**  
Matrikelnummer.: 0426350  
Pramergasse 21/15  
1090 Wien

16. September 2011

(Paulus Naderer)

## Zusammenfassung

Die vorliegende Arbeit stellt Zerstäubungsmessungen von Wolfram mit einer Quartz-Kristall-Mikrowaage vor, welche bereits zuvor an der TU-Wien entwickelt wurde. Mit diesem Messaufbau ist es möglich Massenänderungen von dünnen Schichten von bis zu  $10^{-5}$   $\mu\text{g/s}$  zu detektieren, dies entspricht dem Abtrag von nur  $10^{-4}$  Wolfram Monolagen pro Sekunde.

Wolfram ist in zukünftigen Fusionsexperimenten wie etwa ITER (englisch: International Thermonuclear Experimental Reactor) als eines der Wandmaterialien vorgesehen, vor allem im sogenannten Divertor, wo hohe Belastungen erwartet werden. Um die Beanspruchung der Wolfram Bauteile zu verringern, wird die angrenzende Plasmarandschicht gekühlt. Durch die Beseitigung von Kohlenstoff als Wandmaterial ist diese Kühlung durch intrinsische Verunreinigungen nicht mehr ausreichend, wodurch es notwendig wurde, zusätzliche Fremdstoffe in die Randschicht des Plasmas zu sprühen. Die Verwendung von Stickstoff als Kühlgas konnte z.B. die Belastung der Wolfram Bauteile im Fusionsexperiment ASDEX-Upgrade (Garching, Deutschland) auf tolerierbare Werte reduzieren.

Dadurch ist die Untersuchung des Zerstäubungsverhalten von Wolfram durch Stickstoff-Ionen von erheblichem Interesse. In dieser Arbeit werden sowohl atomare  $\text{N}^+$  als auch molekulare  $\text{N}_2^+$  Stickstoff-Ionen als Projektile verwendet. Beim Vergleich der Zerstäubungsausbeute von molekularen mit gleich schnellen atomaren Ionen konnte eine unerwartete Erhöhung bei der Zerstäubung mit molekularen Projektilen festgestellt werden. Im allgemeinen wird angenommen, dass der Einschlag von  $\text{X}_n^+$  Ionen auf einen Festkörper die gleiche Zerstäubung hervorruft, wie der Aufprall von  $n \cdot \text{X}^+$  Ionen. Die gemessenen Zerstäubungsausbeuten von Wolfram pro Stickstoff Atom sind jedoch bei gleicher Aufprallgeschwindigkeit für molekulare  $\text{N}_2^+$  Ionen um 25% höher als für atomare  $\text{N}^+$  Ionen. Dieser Anstieg in der molekularen Zerstäubungsausbeute wurde nur für Aufprallenergien kleiner als 500 eV pro Atom beobachtet. Die Ergebnisse dieser Messungen gemeinsam mit einer qualitativen Erklärung, basierend auf einem einfachem Model für den Transfer von Energie, werden in dieser Arbeit präsentiert.

## Abstract

This work presents total sputtering yield measurements for tungsten, conducted with a quartz crystal microbalance, which was previously developed at the TU Wien. With this setup it is possible to detect mass changes of thin films as small as  $10^{-5}$   $\mu\text{g/s}$ , which correspond to a removal of only  $10^{-4}$  tungsten monolayers/s.

In future fusion devices like the International Thermonuclear Experimental Reactor (ITER) tungsten is foreseen as one of the first wall materials especially in the divertor, where high power loads are expected. In order to reduce the power load on the divertor target plates the edge plasma is radiatively cooled. After eliminating carbon as first wall material from fusion devices, the radiation due to intrinsic impurities is no longer sufficient, and seeding of additional impurities into the edge plasma region becomes necessary. By using nitrogen as a seeding gas, the power flux onto the divertor plates of the magnetic fusion experiment ASDEX-Upgrade (Garching, Germany) could be reduced to acceptable values.

Therefore sputtering yield measurements of tungsten due to the impact of nitrogen ions are of considerable interest. In this thesis both atomic  $\text{N}^+$  and molecular  $\text{N}_2^+$  nitrogen ions have been used as projectiles. An unexpected pronounced enhancement in molecular sputtering yields when compared to equally fast atomic nitrogen ions could be found. In general, it is often assumed that the impact of an  $\text{X}_n^+$  ion on a solid has the same effect as  $n\cdot\text{X}^+$  ions at the same velocity, especially in the low energy regime. However, measured sputtering yields per atom of molecular  $\text{N}_2^+$  ions are approximately 25% higher than sputtering yields of atomic  $\text{N}^+$  ions at equal impact velocity. This increase in the molecular sputtering yield was observable below impact energies of 500 eV/atom. The results of these measurements together with a qualitative explanation of this enhancement based on a simple energy transfer model, are given in this work.

# Contents

<b>Abbreviations</b>	<b>III</b>
<b>1 Introduction</b>	<b>1</b>
1.1 Fusion energy . . . . .	4
1.2 Magnetically confined plasma . . . . .	6
1.3 Plasma wall interaction and material selection for ITER . . . . .	8
1.4 Plasma edge cooling . . . . .	11
1.5 Outline . . . . .	12
<b>2 Sputtering</b>	<b>14</b>
2.1 Overview . . . . .	14
2.2 Physical sputtering . . . . .	15
2.3 Molecular effects in sputtering . . . . .	20
2.4 Preferential sputtering . . . . .	21
2.5 Potential sputtering . . . . .	22
2.6 Chemical sputtering . . . . .	23
2.7 Computer simulation and fitting . . . . .	24
<b>3 Experimental Setup</b>	<b>27</b>
3.1 The quartz crystal microbalance technique . . . . .	27
3.2 Ion Source and beam alignment . . . . .	34
3.3 Vacuum system . . . . .	42
3.3.1 Operation of ion pumps . . . . .	43
3.3.2 Vacuum system setup . . . . .	44
<b>4 Results and discussion</b>	<b>49</b>
4.1 Beam profile . . . . .	49
4.2 Cleaning of the target surface . . . . .	51

4.3	Sputtering of W by $N_2^+$ and $N^+$ . . . . .	53
4.4	Measured molecular effects . . . . .	57
<b>5</b>	<b>Summary and outlook</b>	<b>59</b>
	<b>Bibliography</b>	<b>62</b>
	<b>List of Figures</b>	<b>69</b>
	<b>Danksagung</b>	<b>72</b>

# Abbreviations

<b>ASDEX</b>	Axially Symmetric Divertor EXperiment
<b>BCA</b>	Binary Collision Approximation
<b>CFC</b>	Carbon Fibre Composite
<b>ECR</b>	Electron Cyclotron Resonance
<b>FC</b>	Faraday Cup
<b>HCI</b>	highly-charged ions
<b>ITER</b>	International Thermonuclear Experimental Reactor
<b>JET</b>	Joint European Torus
<b>PFC</b>	Plasma Facing Component
<b>PLC</b>	Programmable Logic Controller
<b>QCM</b>	Quartz Crystal Microbalance
<b>TSP</b>	Titanium Sublimation Pump
<b>UHV</b>	Ultra High Vacuum

---

*It's like trying to squeeze a balloon full of water:  
The more you squeeze,  
the more it bulges between your fingers.*

*- Daniel Clery in [1]  
visualizing the complexity  
of confining fusion plasmas*

# 1 Introduction

Projections for the world population show a continued increase from the currently around 7 billion people up to 9 billion people on earth by the year 2050 [2]. All these people will need energy, especially people in developing countries will want to use as much energy as we do. Therefore the world wide energy consumption is anticipated to triple in the next 50 years [3].

Today, almost 80% of the worlds energy is produced by burning coal, oil and gas [4]. The combustion of these fossil fuels releases gases such as carbon dioxide. The increase of these gases in the Earth's atmosphere causes an enhanced greenhouse effect resulting in a raise of the global mean temperature. Since the industrial revolution, the average air temperature on Earth has already risen by 0.6 °C [4]. Further extensive use of fossil fuels will then result in a high risk of major climate changes with substantial consequences on the environment due to the release of further carbon dioxide and other greenhouse gases.

Nuclear fission is already widely used with nuclear power plants providing 17% of the worlds electricity demands [4]. Nuclear accidents like the one at the Fukushima nuclear power plant [5] led to the present rejection of nuclear fission in the public opinion. Furthermore the handling and storage of high-level waste is still an unsolved issue. Despite all these problems, nuclear fission remains one of the large scale sources for electric power generation, beside hydro power, that does not produce carbon dioxide.

Renewable energy sources such as wind, solar, tidal, and geothermal energy presently account for less than 0.7% of our worldwide electricity production [4]. Up to now the high costs in producing energy from renewable sources prevented further expansions. But with rising costs of fossil resources they become more and more competitive on the



## 1 Introduction

---

global market. However, renewable energy sources are not capable of producing the constant and reliable baseload power that cities need [1].

A fusion power plant would have great advantages compared to the other energy sources mentioned above. Unlike the burning of fossil fuels like coal, a fusion power plant would not emit greenhouse gases. Therefore fusion power plants would have significantly less negative effects on the environment. The fuels for nuclear fusion power plants, deuterium and tritium, are readily available and nearly inexhaustible. The performance of a well designed fusion power plant would be economically outstanding since 1 kg of deuterium-tritium fuel per day would be enough to secure the operation of a 1 GW fusion plant whereas a 1 GW coal-fired plant would burn about 10 000 tons of coal during the same time [1]. Unlike renewable energy sources such as wind or solar power, fusion energy would also be able to provide a steady and reliable baseload power. Compared to nuclear fission power plants, the two major issues, safety and nuclear waste disposal, are certainly less problematic. At a nuclear fusion power plant, an accident with a runaway reaction is not possible since, at a given time, only a small amount of fuel is present in a fusion reactor [1]. Nuclear fusion would produce only rather short lived radioactive waste with half live periods in the range of 10 to 20 years. Thus, after a storage period of about 100 years, we would be able to recycle already used components again [6].

The biggest fusion device in operation up to now is the Joint European Torus (JET) in the United Kingdom, which managed to produce 16 MW of fusion power in the year 1997 [8]. However this was only 65% of the power needed to keep the reaction running. The next step towards a fusion power plant is the construction and operation of the International Thermonuclear Experimental Reactor (ITER) in the south of France. The construction work on the ITER site began in 2007 and will be finished in 2018 with the first operations in 2019 [9]. The official goal of ITER is 'to demonstrate the scientific and technological feasibility of fusion power for peaceful purposes' [10]. The advised construction and operation costs of about 12 billion dollar [1] provoked a lot of criticism, but since ITER is a global project these cost are shared among the governments of the European Union, China, India, Japan, South Korea, Russia and the United States, which are working together on this project. ITER will have to show that it is possible to suitably produce energy from fusion in a steadily, continuous way so that it can be used commercially in the future for a fusion power plant.

By increasing the size of the tokamak (ITER will be twice the size of JET) it will be

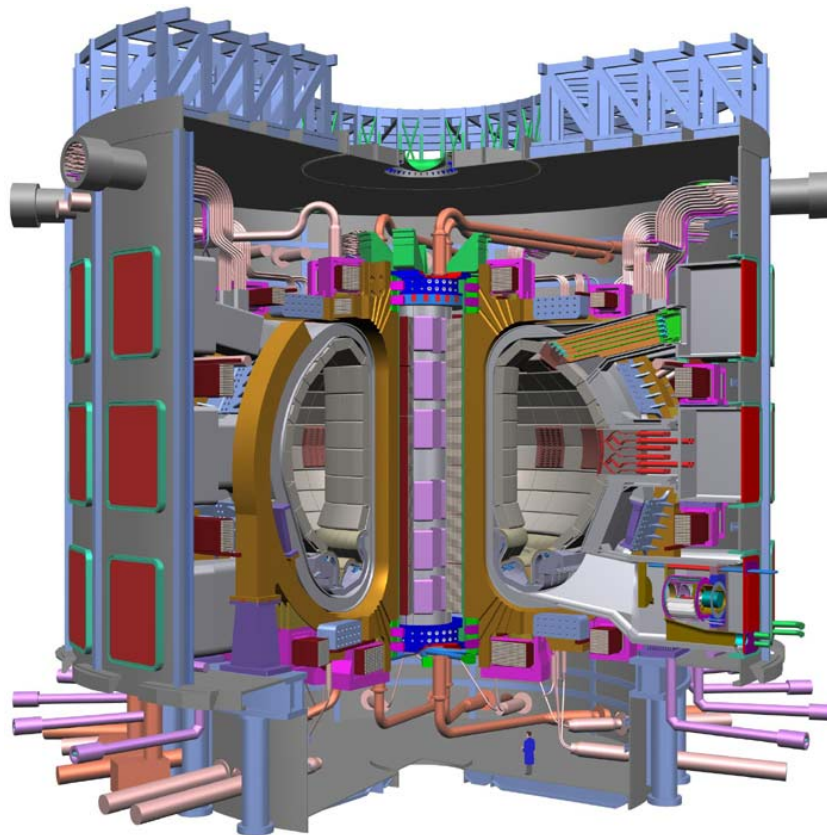


Figure 1.1: Schematic drawing of ITER: The woman at the bottom shows the scale of this machine (Picture taken from [7])

possible for the first time to produce net energy from fusion processes. ITER is designed to produce 500 MW of fusion power, which is ten times more than needed to keep the fusion processes running [10]. The key to this net power production is a self-sustaining plasma, which means that most of the plasma heating, necessary to keep the plasma burning, comes from the fusion processes themselves. This burning plasma will be achievable inside the ITER vessel for the first time and scientist will have to learn how to produce, control and sustain this burning plasma. Another key objective for this new fusion device, is to implement and test components, needed for future power plants, e.g. superconducting magnets or remote handling of the components. In a second operation stage of ITER, the main focus will be on the breeding of tritium from lithium inside the wall material surrounding the plasma [9].

## 1.1 Fusion energy

The energy released by nuclear fusion reactions is referred to as fusion energy. In a fusion reaction two light nuclei join and form a heavier nucleus. The mass of the separated protons and neutrons (which are the constituents of atomic nuclei) is greater than the mass of the bound nucleus. This difference in the mass, the so-called mass defect, is released in form of kinetic energy of the reaction products according to Einstein's relation  $E = mc^2$ . This energy is a measure of the forces that hold the nucleus together and is known as binding energy. As long as the masses of the two reactants are lower than the mass of iron (which has the largest binding energy per nucleon) fusion processes release energy. The converse process, nuclear fission, releases energy as long as the mass of the nucleus is heavier than the mass of iron.

To initialise a fusion process the two light nuclei have to be brought together close enough so that the short-ranging nuclear forces can overcome the long-ranging, repulsive, electrostatic force. In stars, the conditions necessary for a nuclear fusion reaction to occur are naturally provided by gravitational forces compressing the reactants in a small region in space. In laboratories here on earth, the two atoms are heated up so that the thermal energy of the reactants is sufficient to tunnel through the Coulomb barrier in a collision - this type of fusion is called thermonuclear fusion. By this all or most of the electrons are stripped from the atom. The ionised gas containing positively charged nuclei and negatively charged electrons is also called a plasma. In handling such a plasma, a big advantage compared to a neutral gas is that it can be affected by means of electromagnetic fields. Since the Lorentz force, acting on a charged particle, is always perpendicular to its velocity, ions and electrons gyrate around magnetic field lines. A mesh of closed magnetic field lines can therefore be used to isolate the hot plasma from the relatively cold vessel walls in order to retain the energy from fusion processes as long as possible.

The confinement time of the particles  $\tau_E$ , the plasma density  $n$  and the temperature  $T$  are the key parameters of a fusion reactor. These three parameters form the so-called 'fusion triple product', a figure of merit for fusion devices. It is based on a power balance calculation published by Lawson [11], which compares the released energy of thermonuclear fusion reactions with its losses. By this Lawson was able to define the key parameters needed for a self-sustaining system. The released fusion energy depends on the density

of the two gases, their reaction cross section averaged over their Maxwellian velocity distributions (thermonuclear fusion) and the energy released in one reaction [11]. As we are talking about thermonuclear fusion, the reactants have a distribution of velocities and so it is reasonable to average the cross section over the velocity distribution. The reaction rate, that is fusion per volume per time, is then given by the product of this average and the number densities of the two reactants.

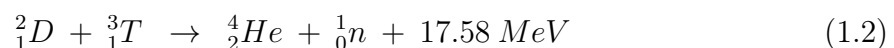
$$f = n_1 n_2 \langle \sigma v \rangle \quad (1.1)$$

Energy can be lost either by conduction or radiation as bremsstrahlung. The Lawson criterion defines certain conditions for the triple product  $\tau_E \cdot n \cdot T$ , where the fusion would reach ignition, i.e. where the energy produced in the fusion reactions exceeds the energy needed to sustain these conditions. For a sustained D-T fusion reaction inside JET the following plasma conditions [12] have to be maintained simultaneously:

- plasma temperature  $T$ : 100 - 200 million Kelvin, i.e. about 10 keV
- energy confinement time  $\tau_E$ : 4 - 6 seconds
- central density in plasma  $n$ :  $1 - 2 \cdot 10^{20}$  particles/m<sup>3</sup> (approx. 1/1000 gram/m<sup>3</sup>, i.e. one millionth of the density of air)

The most promising fusion process achievable in a fusion reactor on earth is the fusion of the two hydrogen isotopes deuterium ( ${}^2_1D$ ) and tritium ( ${}^3_1T$ ) to a helium nucleus, since it has the highest fusion reaction cross section at the lowest temperature. This can be seen by looking at figure 1.2, where three different fusion reactions are compared by plotting the reaction rate versus the temperature.

The fusion process of these two hydrogen isotopes generates a helium nucleus ( ${}^4_2He$ ) and a neutron ( ${}^1_0n$ ) and releases about 17.58 MeV of fusion energy.



The generated neutron, not affected by the magnetic field, transports four fifth of the total released energy to the wall materials where this energy is converted into heat and subsequently into electrical power. The residual energy, carried by the helium nucleus, is transferred to other particles in the plasma by collisions thus heating the plasma once the

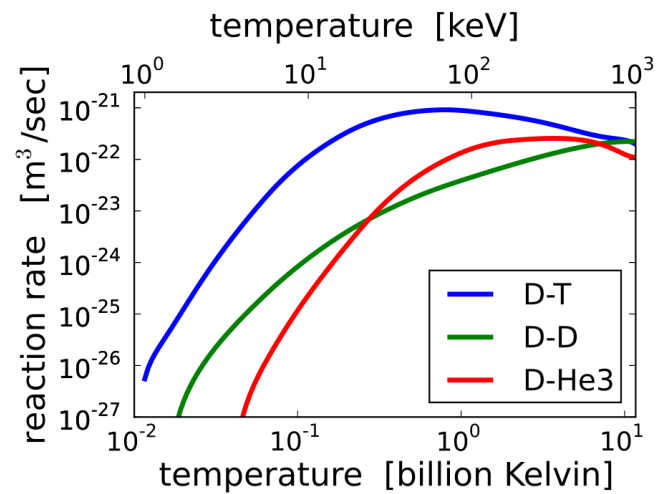


Figure 1.2: Reaction rate versus temperature: Compared with other fusion reactions, the D-T reaction has the highest reaction rate at the lowest temperature. (Picture taken from [13])

conditions for fusion are reached. If the resulting heating power is sufficient to sustain the temperature of the plasma and to compensate for the energy losses, we would end up with a burning plasma and would be able to extract more energy from the system than we would need to provide to keep it running.

Deuterium occurs with a natural abundance of about 0.015% in seawater and can be easily extracted. Tritium decays with a half-life time of 12.5 years but can be bred from the abundant light metal lithium by neutron bombardment. This can be done still inside the fusion reactor, by adding reasonable amounts of lithium to the wall materials. Both fuelling elements are therefore available on earth in large quantities.

## 1.2 Magnetically confined plasma

A magnetically confined plasma is an anisotropic and complicated medium. For many decades various magnetic plasma confinement devices have been built and operated around the world. The most developed device up to now is the tokamak, which is a Russian abbreviation meaning 'toroidal chamber with magnetic confinement'. The basic design of a tokamak is a torus (or doughnut) shaped vacuum vessel, which is enfolded by

## 1 Introduction

toroidal coils [14]. These coils generate a circular magnetic field that loops around the torus. This kind of magnetic field lines alone would not be sufficient to confine ions and electrons since both of them would also drift outwards, away from the axis of rotation due to a decrease of the magnetic field in outward direction. A second, poloidal field is needed to generate helical magnetic field lines (cf. figure 1.3). Thereby the above-mentioned outward drift of both electrons and ions is compensated. The poloidal field is produced by the plasma current induced by a solenoid in the center of the torus. The plasma current, beside radiofrequency heating and neutral beam injection, is also used to heat up the plasma to a temperature of about 10 to 20 keV to start and sustain the fusion process.

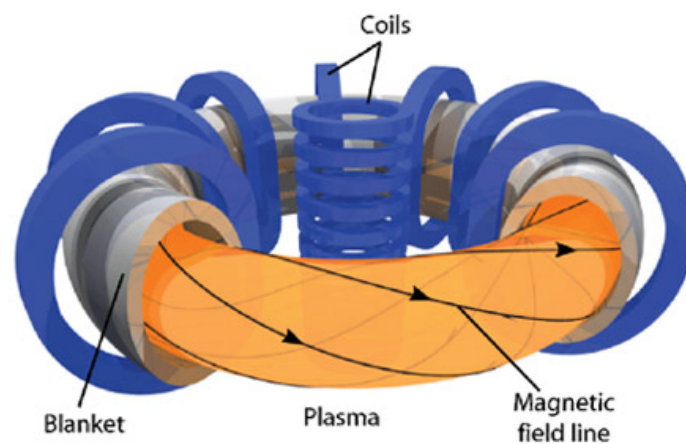


Figure 1.3: A schmeatic drawing of a tokamak with poloidal and toroidal coils and the resulting helical magnetic field lines (Picture taken from [15])

In the center of the torus the magnetic field lines are closed and charged particles can be confined for a certain time. However the confinement of such a magnetic trap is imperfect and energy (heat) and particles radially diffuse outwards. As a result particles and quantities of energy move towards the plasma edge, where the magnetic field lines are not closed anymore. These field lines are intersected by Plasma Facing Components (PFCs). A robust and long-living design of these PFCs is one of the biggest challenges in building a fusion power plant since these components will have to withstand extreme heat loads and particle fluxes.

In the early days of fusion research limiters, usually very robustly made, were positioned on the outer and inner wall, to protect more delicate structures from particle impact. In the mid 1970ies the divertor concept, was introduced in various tokamaks, which allowed

to pump impurities, especially the helium ash from the fusion processes, more efficiently. The original purpose of the divertor was to separate the source of impurity production from the main plasma by arranging that the primary plasma-material interaction occurs in a separate chamber [16]. This separation is done with an auxiliary magnetic coil situated near the divertor, which modifies the magnetic field lines at the bottom and generates a well defined cut between the confined and the not confined particles.

Figure 1.4 shows a cross section of the ITER vacuum vessel in which the outermost magnetic field lines are sketched. The boundary between closed and open field lines is called separatrix or Last Closed Flux Surface (LCFS). Particles inside the separatrix are confined by the closed magnetic field lines, whereas particles outside of the separatrix will impinge onto the PFCs, especially onto the divertor target plates. The plasma region outside the separatrix is called scrape of layer (SOL) since these particles will be removed from the plasma edge. Ions from this plasma region impinge on the divertor especially around the strike point, where they are neutralised and eventually cause sputtering. The sputtering of wall material adds impurities to the plasma and has to be prevented as efficiently as possible. Especially high  $Z$  impurities would dilute the hydrogen plasma and thereby reduce its density as well as lead to radiation losses. The amount of tolerable impurities inside the plasma is therefore restricted. The magnetic field configuration in the divertor region, prevents particles from re-entering the core plasma and forces them to return to the divertor plates. Most of the tokamak machines now use limiters for the start-up phase and a divertor to operate the tokamak in various confinement modes.

### 1.3 Plasma wall interaction and material selection for ITER

The interaction of the plasma with the PFCs is determined by various plasma parameters, power and particle fluxes, and is most intense in the vicinity of the 'strike point' (cf figure 1.4), where the separatrix intersects the divertor target plate [17]. On the other hand, plasma wall interactions of the edge plasma with the surrounding walls affect the conditions in the core plasma and have great influence in the operation of a tokamak. This interdependency, between the plasma and the wall components surrounding it, has to be kept in mind when choosing materials for the PFCs.

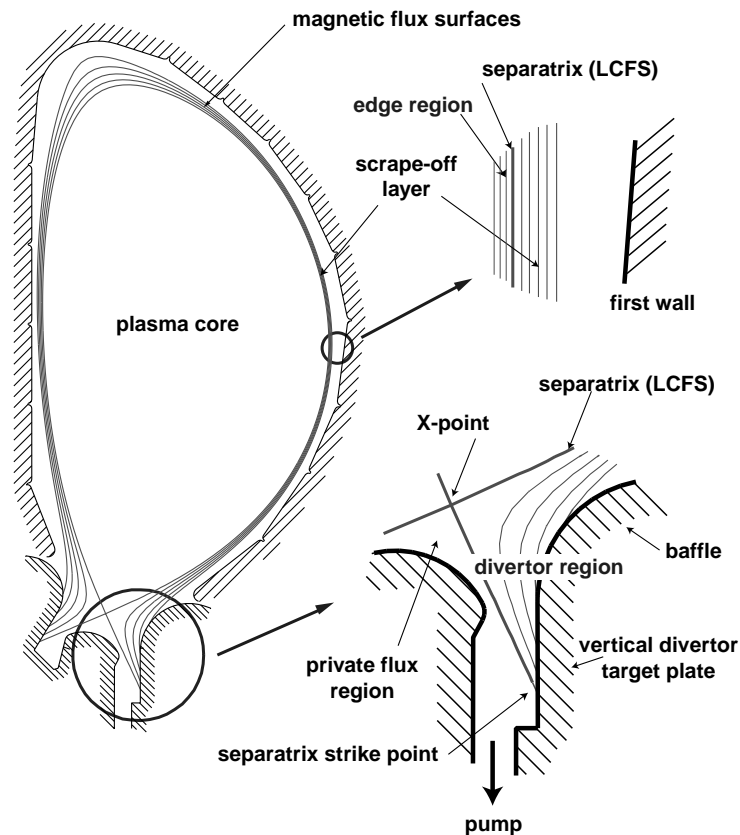


Figure 1.4: Sectional view of the ITER tokamak with sketched magnetic field lines: The separatrix or last closed flux surface (LCFS) separates the plasma core from the scrape of layer (SOL) (Picture taken from [17])

The selection of the materials for the PFCs is mostly a compromise between the requirements of plasma performance (e.g. need to minimize impurity contamination) engineering integrity, component lifetime (e.g. need to withstand thermal stress, acceptable erosion, material changes due to high neutron fluxes) and safety (e.g. need to minimize tritium and radioactive dust inventories) [17]. At different regions inside the vessel of ITER different PFC materials are selected due to different plasma conditions.

The inner wall of the vacuum vessel is covered with a so-called blanket that protects the vacuum vessel and the surrounding magnets from neutron impact and heat fluxes from the fusion processes. In the blanket the neutrons are slowed down by collisions with the wall material which leads to a temperature increase in the blanket modules. This heat is then dissipated by a coolant and used to produce electric energy. In ITER the inner walls of the blanket modules will be made of beryllium. Since beryllium is a



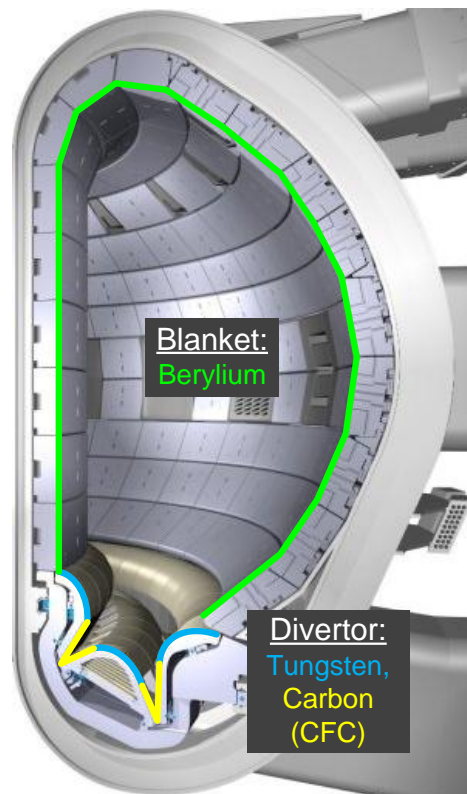


Figure 1.5: ITER wall materials: The blanket modules will be made out of beryllium. For the divertor carbon in form of CFC and tungsten will be used (Picture taken from [9])

low-Z material, impurities, which have been sputtered into the plasma, are easily ionized without significant energy losses. Beside that it is an excellent oxygen getter and can also help to suppress chemical erosion of carbon [17].

In the first stage of ITER operation the divertor, located at the bottom of the vacuum vessel, will partly be made of carbon, in form of Carbon Fibre Composite (CFC). Especially, for the lower parts of the divertor, where the particle flux is most intense, carbon will be used, due to its good power handling and thermal shock resistance. Carbon does not melt (but is subjected to sublimation) and is able to preserve its shape even under extreme temperatures [17]. However carbon is eroded by chemical sputtering which leads to a reduced lifetime of the components, material migration and co-deposition of tritium with the eroded carbon. Large tritium inventories, due to the carbon co-deposition, are a major safety concern for ITER, which is why it is planned to switch to an all tungsten design before actually starting experiments using tritium in ITER.

Near the baffle region of the divertor (cf figure 1.4), an interface between the relatively hot plasma in the reactor core (energy  $> 100$  eV) and a high neutral density inside the divertor [17] is located. In this region it is expected that particles with energies up to several keV will impinge onto the PFCs and cause a substantial amount of sputtering. Thus tungsten (a high  $Z$  material) was chosen since it has a very low sputtering yield and a high energy threshold for physical sputtering [18], although acceptable tungsten impurity concentrations within the plasma core are very low.

Removing the power from PFCs under high heat load is another key issue for ITER. During normal operation scenarios the PFCs will be exposed to heat loads of typically  $0.5 \text{ MW/m}^2$  at the first wall and up to  $20 \text{ MW/m}^2$  at the divertor [19]. Melting of the components can only be avoided by efficiently cooling them. Therefore the thermal resistance and hence the distance between coolant and the PFCs has to be kept as short as possible. The cyclic operation of the fusion device results in a cyclic thermal heat load with thermal fatigue damage and reduced lifetime of the component. A major topic in fusion research of recent years was the improvement of joining technologies between armour material (Be, C, W) and copper alloys, which provide the heat sink for the cooling [20].

## 1.4 Plasma edge cooling

**(parts of this section will appear in [21])**

Even small amounts of tungsten impurities can have large effects on the performance of a fusion experiment. As tungsten is a high- $Z$  material, it can abstract significantly more energy from the plasma due to ionisation processes as compared to low- $Z$  materials. In addition, not fully ionised tungsten ions would reduce the energy of the plasma by line radiation. Therefore, the sputtering of tungsten has to be avoided as efficiently as possible.

Intrinsic impurities, from PFC made of carbon, can reduce the energy of incoming particles. When a neutral or a not fully ionised impurity atom enters the divertor plasma, it will be ionised to higher charge states and line radiation will be emitted [22]. In this way power loads on divertor target plates are reduced. In the close vicinity of the strike point (cf. figure 1.4) momentum losses due to recombination and charge exchange of

hot ions with cold impurities can further reduce peak power loads on the divertor target plate [22].

By coating fusion vessels completely with tungsten, in fusion devices like ASDEX Upgrade, impurity concentrations within the plasma were decreased considerably [23]. With the elimination of carbon as a PFC however, the radiation due to intrinsic impurities is no longer sufficient. It has thus become necessary to seed additional impurities. In ASDEX Upgrade plasma edge cooling by seeding impurities into the edge region of the plasma is now used to reduce erosion of divertor plates [23]. A similar approach is foreseen for the ITER like wall in JET, where beryllium walls and a tungsten divertor are expected to lead to reduced intrinsic radiative levels [24]. Beside several noble gases especially nitrogen in conjunction with the tungsten coating proved to be a suitable impurity species in ASDEX Upgrade. The use of nitrogen resulted not only in the desired divertor power load reduction but also in improved energy confinement and overall plasma performance [25]. Particularly due to its radiative capability below 10 eV, nitrogen turned out to be a suitable replacement for carbon as a divertor radiator [22].

It is hence of considerable interest to find out as much as possible about the interaction of nitrogen containing plasmas with tungsten surfaces. In the literature (cf. [26] and [27]) investigations of tungsten sputtering by nitrogen are summarised but the available database is scarce compared to other projectile-target combinations.

Recent experiments conducted by Schmid et al [28] showed unexpectedly low sputtering yields of tungsten under nitrogen bombardment. The authors in [28] have studied the sputter erosion of tungsten by high fluxes of  $N_2^+$  projectiles and observed the formation of a tungsten-nitride surface layer within the ion penetration depth. As a result of the nitrogen accumulation in these layers a reduced partial sputtering yield of tungsten as compared to a pure tungsten surfaces was found [28].

## 1.5 Outline

This thesis describes sputtering yield measurements of tungsten by the bombardment of various nitrogen ions under controlled laboratory conditions using a Quartz Crystal Microbalance (QCM) technique. The so-obtained measurements are compared with

previous sputtering yield measurement and computer simulations. The high accuracy of our experimental setup allowed us to investigate differences in the sputtering yield due to bombardment by atomic and molecular nitrogen projectile ions (i.e. a so-called molecular effect) in detail. A phenomenological together with an analytical description of physical sputtering processes is given in chapter 2. A short description of chemical sputtering as well as potential sputtering together with a section concerning molecular effects in sputtering can also be found in there. Chapter 3 gives an overview of the experimental setup also including a section about the renewal of the vacuum system, which was done in the course of this thesis. Obtained measured data and a discussion of the investigated molecular effect can be found in chapter 4. Finally a short summary and an outlook are given in chapter 5.

Parts of this work have been presented as a poster

**P. Naderer**, K. Dobes, N. Lachaud, C. Eisenmenger-Sittner and F. Aumayr; 'Sputtering of tungsten by  $N^+$  and  $N_2^+$  ions - investigation of molecular effects', 13th International Workshop on Plasma-Facing Materials and Components for Fusion Applications, Rosenheim, Germany, 11.5.2011

The results obtained during this diploma thesis are going to be published in the journal *Physica Scripta*.

K. Dobes, **P. Naderer**, C. Eisenmenger-Sittner and F. Aumayr; 'Sputtering of tungsten by  $N^+$  and  $N_2^+$  ions - investigation of molecular effects', *Physics Scripta*, (2011) in print

This is indicated by a small note after the individual section heading.

## 2 Sputtering

### 2.1 Overview

The ejection of target atoms from a solid surface due to the impact of impinging projectiles is called sputtering. Aside from ions the incoming projectiles can also be neutral atoms, neutrons, electrons or clusters of atoms. The erosion rate is measured by the total sputtering yield  $Y$ , which is a stochastical variable. It is defined as the mean number of atoms removed from the solid target per incident projectile.

$$Y = \frac{\textit{atoms removed}}{\textit{incident particle}} \quad (2.1)$$

The sputtering yield depends on the energy, the mass and angle of incidence of the incoming particle, furthermore on the mass of the target atoms, the crystallinity and the crystal orientation of the solid and on the surface binding energy of the target. In general, it is however nearly independent of the target temperature [29].

Beside physical sputtering, which is a result of the transfer of kinetic energy from the incident particle to the target atom, also chemical sputtering [27] and potential sputtering [30] are known sputter processes. If the projectiles are chemically reactive, chemical effects have to be considered additionally to the physical sputter processes [27]. These chemical reactions can either increase or decrease the sputtering yield depending on the binding strength of the newly formed species. Potential sputtering refers to sputter processes where the removal of target particles is initiated by the potential energy of the projectile. The potential energy of a multiply charged ion is the sum of all ionization energies, which were necessary to generate this multiply charged ion. Potential sputtering effects can usually only be observed for the impact of slow, multiply-charged ions on electrically insulating target materials [30].

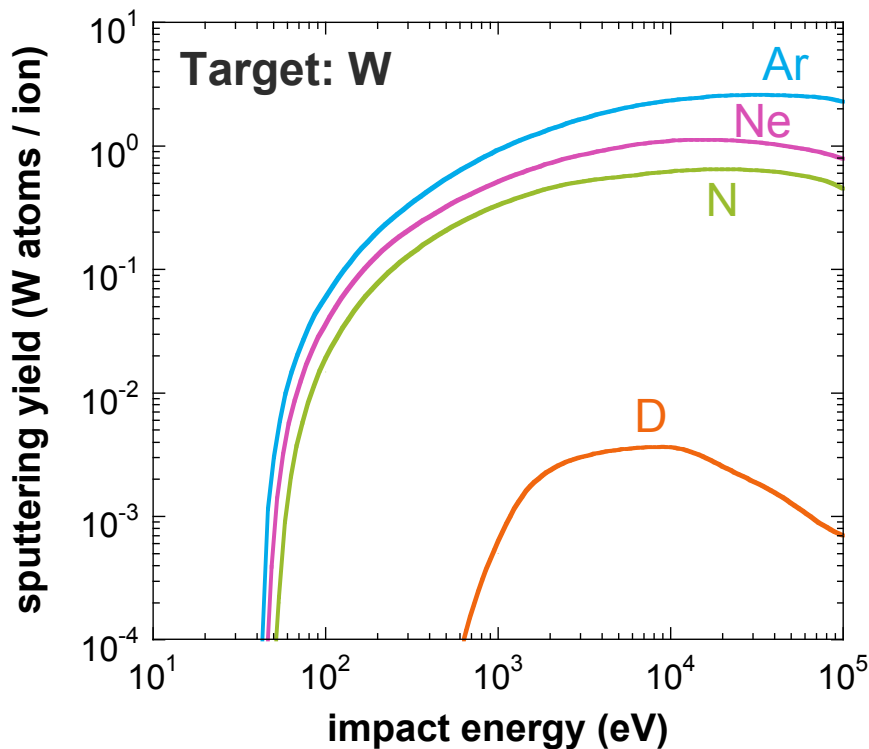


Figure 2.1: Typical dependence of the sputtering yield of tungsten due to the impact of either argon, neon, nitrogen or deuterium ions simulated with TRIDYN [32] in static mode.

## 2.2 Physical sputtering

### Phenomenological description

The projectile transfers its kinetic energy and momentum via elastic collisions to target atoms. With each collision the energy of the projectile decreases and it might also be deflected. If the energy transferred to a recoiling target atom in such a collision is higher than the binding energy to the lattice, it can leave their positions and collide with further target atoms. Sputtering is therefore a multiple collision process involving a cascade of moving target atoms [31]. A scattered atom is sputtered if its position is close to the surface and the component of the transferred energy normal to the surface is greater than the surface binding energy [29].

Figure 2.1 shows the sputtering yield of tungsten depending on the energy of the incom-

## 2 Sputtering

---

ing particles ( $\text{Ar}^+$ ,  $\text{Ne}^+$ ,  $\text{N}^+$  and  $\text{D}^+$ ) calculated with the program TRIDYN (see details on page 24). As can be seen in figure 2.1, the sputtering yield varies strongly with the kinetic energy but also with the mass of the projectiles.

Below a certain threshold energy (typically in the range of a few eV up to 400 eV) no physical sputtering takes place, because in this energy regime the kinetic energy of the projectile does not suffice to release target atoms from their lattice sites. This threshold energy can be analytically approximated by

$$E_{th} = \frac{(m + M)^4}{4 m M (m - M)^2} E_s \quad (2.2)$$

with  $m$  and  $M$  being the projectile and the target mass respectively and the surface binding energy  $E_s$  [33].

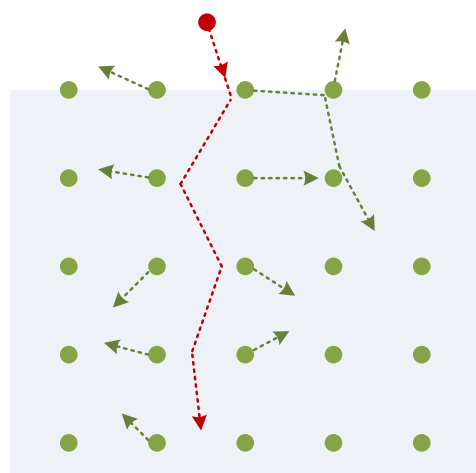
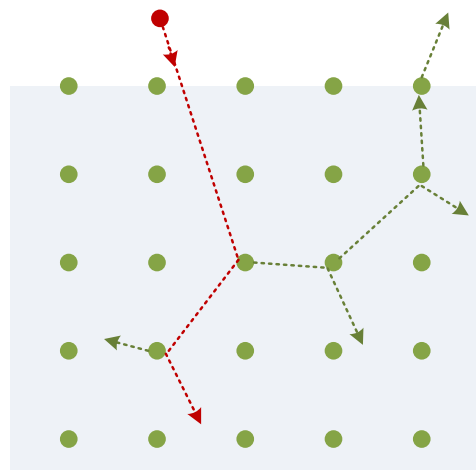
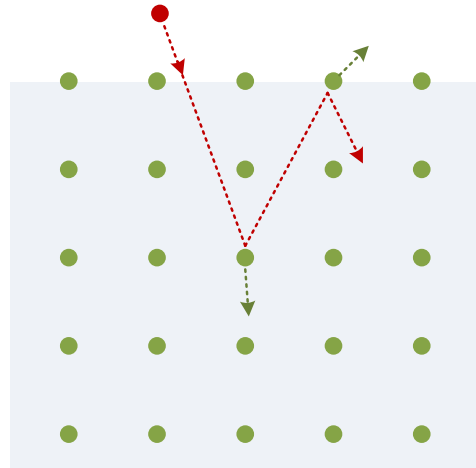
projectile name	threshold energy for kinetic sputtering
$\text{D}^+$	409 eV
$\text{N}^+$	45 eV
$\text{Ne}^+$	38 eV
$\text{Ar}^+$	36 eV

Above this threshold energy, the yield increases with incident energy and reaches a broad maximum at impact energies between 10 keV and 100 keV. With increasing energy the projectile range in the target material increases since it is a function of the energy. Thus more and more collisions occur far away from the target surface and a lot of recoiling target atoms do not reach the surface of the solid. For higher energies, the sputtering yield decreases again with projectile energy.

The literature (e.g. [29]) distinguishes between three qualitatively different situations in elastic collisions, depending on the energy of the incoming particle:

## 2 Sputtering

- Single-knockon regime:** The incoming particle transfers its energy to several target atoms. These target atoms can be sputtered either directly or after undergoing a small number of further collisions, as long as the transferred energy is greater than the binding energy. Sputtering with light projectiles or generally low energy ions (eV to keV) fall into this category [34].
- Linear cascade regime:** In this energy regime the scattered target atoms are energetic enough to generate secondary and higher-generation recoils [29]. As the density of this collision cascade is low, target atoms are in equilibrium before they are hit by recoil atoms and the collisions can be described by a binary collision theory. This collision cascades are initialized in the medium energy range (keV up to MeV).
- Spike regime:** In the spike regime secondary and higher order recoil atoms are formed similarly to the linear cascade regime. The difference to the linear cascade regime is, that the spatial density of moving atoms is much higher. Therefore, target atoms are already excited and deflected from their equilibrium position before they are hit by lower order recoils. This leads to nonlinear effects, which can be especially observed for the impact of fast (MeV - GeV), heavy ions [29].





## Analytical description

As already mentioned, in the beginning of this chapter a measure for the erosion rate is the total sputtering yield  $Y$ , which is the mean number of emitted atoms per incoming particles. A theoretical description of physical sputtering, capable of calculating the sputtering yield, was first given by Sigmund [35] in 1969 using integral transport equations. If the collisions between the initial projectile and the target atoms occur rarely (as it is the case in the linear cascade regime), it can be assumed that these collisions, are a sequence of independent, binary collisions, between the projectile and target atoms or target atoms and higher order recoils. This approach in calculating collision phenomena is called the Binary Collision Approximation (BCA). It is used by many simulation programs (cf. section 2.7).

The sputtering yield, for particles impinging perpendicularly to the target surface, can be expressed by

$$Y = \Lambda F_D(E_0) \quad (2.3)$$

with  $\Lambda$ , a materials factor, characterizing the target material properties such as the surface binding energy [36]. The other factor in this equation ( $F_D$ ) summarizes the energy deposited per unit length, which depends on the type, energy and direction of the incident ion and a few target parameters [29]. This factor can be written in the form

$$F_D(E_0) = \alpha \cdot NS(E_0) \quad (2.4)$$

where  $\alpha$  is a dimensionless correction factor depending on the angle of incidence, the mass ratio of target  $M$  and projectile  $m$  mass and the ion energy. The product of the atomic density  $N$  of the target and the stopping cross-section  $S(E_0)$  is equal to the energy-loss rate per unit depth interval

$$NS(E_0) = \frac{dE}{dx} \quad (2.5)$$

This energy loss rate of an energetic ion moving through a solid can be split into energy losses from nuclear collisions ( $n$ ) and losses from electronic collisions ( $e$ ).

$$\frac{dE}{dx} = \left. \frac{dE}{dx} \right|_n + \left. \frac{dE}{dx} \right|_e \quad (2.6)$$

## 2 Sputtering

These two energy-loss mechanisms depend on the energy  $E_0$  and atomic number  $Z$  of the projectile: nuclear stopping is predominant for low  $E_0$  and high  $Z$ , whereas electronic stopping takes over for high  $E_0$  and low  $Z$  [36]. Figure 2.2 shows both, the nuclear and the electronic stopping power for argon and nitrogen ions in tungsten.

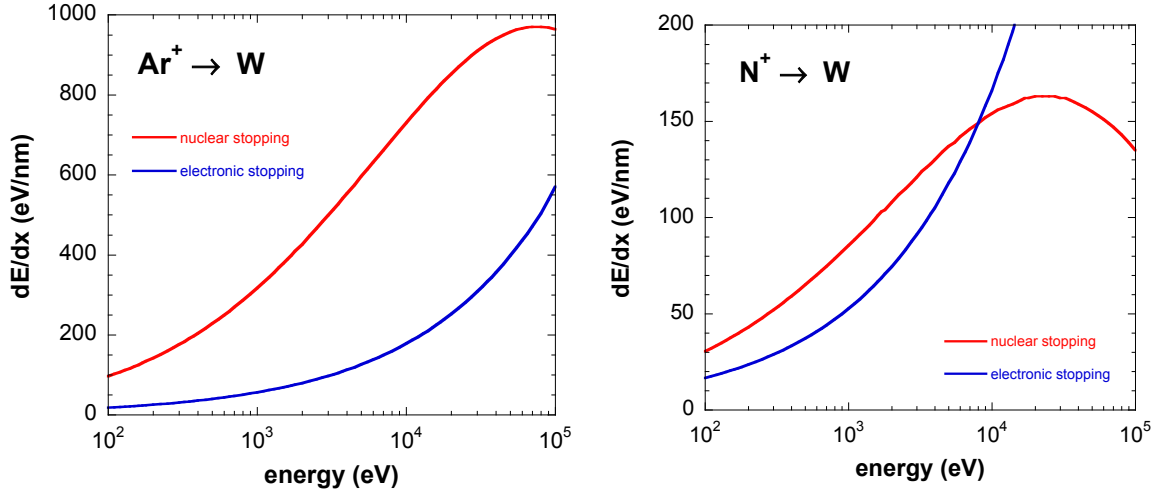


Figure 2.2: Nuclear and electronic stopping power for argon and nitrogen ions in tungsten as calculated using SRIM 2008 [37].

In a first approximation only elastic, nuclear collisions are considered, neglecting energy losses from inelastic electronic collisions like the excitation of target atoms. The energy-loss rate of the ion on its way through the target is therefore determined by the nuclear stopping power given by

$$\left. \frac{dE}{dx} \right|_n = N \int_{T_{min}}^{T_M} T \frac{d\sigma(E_0)}{dT} dT \quad (2.7)$$

In this equation  $E_0$  is the energy of the ion and  $T$  is the energy transferred to the target atom in a binary collision. The integration limits  $T_{min}$  and  $T_M$  are set by the minimum and maximum of transferable energy. In an elastic head-on collision, the maximum transferable energy for a projectile with mass  $m$  and kinetic energy  $E_0$  onto a target atom with mass  $M$  is given by

$$T_M = \frac{4 m M}{(m + M)^2} \cdot E_0 \quad (2.8)$$

With equation 2.5 the stopping cross section is defined. In the approximation of elastic, nuclear collisions we can define the nuclear stopping cross section given by

$$S_n(E_0) = \frac{1}{N} \frac{dE}{dx} \Big|_n = \int_{T_{min}}^{T_M} T \frac{d\sigma(E_0)}{dT} dT \quad (2.9)$$

In equation 2.7 and 2.9 the term  $\frac{d\sigma(E_0)}{dT}$  gives the differential energy-transfer cross-section for a collision between projectile and target. The differential energy-transfer cross-section can be derived from the following equation [36]

$$\frac{d\sigma(E_0)}{dT} = \frac{4\pi}{T_M} \frac{d\sigma(\theta_c)}{d\Omega} \quad (2.10)$$

where  $T_M$  is again the maximum energy that can be transferred in the collision,  $\theta_c$  is the scattering angle and  $\frac{d\sigma(\theta_c)}{d\Omega}$  is the angular scattering cross-section for a certain projectile-target combination. To calculate cross-sections for atom-atom collisions, screened coulomb potentials are used. These potentials take into account that the positive charge of the nucleus is partially screened by the electrons in the shell of an atom. Therefore, to calculate sputtering yields, at first the nuclear stopping cross-section and from that the energy deposited per unit length  $F_D(E_0)$  have to be determined which directly leads to the sputtering yield [36].

## 2.3 Molecular effects in sputtering

(parts of this section will appear in [21])

The differences between the spike regime and the linear cascade regime become visible by comparing the bombardment of diatomic molecular ions with atomic ions. In general molecules that approach the target surface will dissociate almost immediately [29] upon surface impact. In the linear cascade regime, the low density of the collision cascade allows a superposition of the two cascades induced by the two constituents of the molecule and the sputtering yield will be approximately twice that for bombardment with atomic ions [29]. Thus in the linear cascade regime of sputtering it is assumed that the impact of a  $X_n^+$  ion on a solid has the identical effect as  $n \cdot X^+$  ions at the same impact velocity. This is different for the spike regime. With the high density of moving atoms yielding

a high energy density in the collision cascade, the superposition of the two collision cascades loses its validity and nonlinear effects arise. These nonlinear effects in the collision cascade cause enhanced molecular sputtering yields, so-called 'molecular effects'. Andersen et al ([38], [39] and [40]) observed such molecular effects on Ag and Au under the impact of fast (200-400 keV) and heavy (Te) ions. They also could show a trend consistent with the theory, namely that for a fixed target, the heavier the projectile, the larger is the molecular effect, and similarly, for a fixed projectile, the heavier the target, the larger is the molecular effect [39].

Very little is known, however, about molecular effects close to the sputtering threshold ( $< 1$  keV). Yao et al [41] have reported the first observations of a sputtering enhancement for molecular projectiles as compared to atomic ions at very low projectile energies. They investigated the sputtering yield from a gold surface under the impact of molecular and atomic nitrogen and oxygen ions and found that for energies below 500 eV the  $N_2^+$  sputtering yield diverged noticeable from the corresponding  $N^+$  yield. Yield enhancements of almost a factor 4 have been found at projectile kinetic energies of 50 eV [41]. A molecular effect has also been reported for chemical sputtering of graphite by low energy atomic and molecular hydrogen and deuterium projectiles [42] as well as for erosion of a-C:H thin films by hydrogen ions [43].

In this diploma thesis molecular effects for the sputtering of tungsten due to the impact of nitrogen ions are reported. These molecular effects are observed by comparing the sputtering yield measurements of  $N_2^+$  ions with  $N^+$ . The results together with a qualitative explanation following the arguments presented by Yao [41] can be found in section 4.4.

## 2.4 Preferential sputtering

Sputtering becomes more complex if multicomponent targets are involved. In this case preferential sputtering, i.e. favoured sputtering of one component, can be observed. In a multicomponent target, the partial sputtering yield  $Y_i$  is defined in the usual way as the ratio of the sputtered atoms of species (component)  $i$  per projectile [27].

At the beginning of the sputtering process, the surface concentrations of the constituents

Figure 2.3: Mean ion range of nitrogen ions in tungsten as calculated using SRIM 2008 [37].

are equal to those in the bulk. But the individual components of the target need not to be sputtered stoichiometrically, i.e. in proportion to their concentrations [44], which can eventually lead to a change in the surface composition. This is called preferential sputtering. It is a result of the fact that the energy transfer, from the projectile to the different target atom species, is not necessarily equally efficient. In addition to that, in general the two components have different surface binding energies, which also influences the partial sputtering yields.

Preferential sputtering of one species then leads to the formation of a surface layer with a composition profile different from the bulk composition and enriched in the not preferentially sputtered target species. This enrichment finally leads to a shift of the partial sputtering yields in the opposite direction. The composition changes proceed with bombardment until at some incident fluence a steady state or equilibrium is reached [44]. Although the target thickness will further decrease under ion bombardment, the depth profile will not change anymore with increasing fluence [27]. Steady state conditions are in general reached after a surface layer with a thickness of the order of the ion penetration depth (see figure 2.3) has been removed.

## 2.5 Potential sputtering

In addition to the kinetic energy, ions may also carry potential energy. The potential energy of an ion with charge state  $q$  equals the sum of the binding energies of the  $q$  electrons that had to be removed to produce the ion. This potential energy can be rather large for high values of  $q$ . Effects of potential sputtering on certain target species can therefore become visible especially for slow, highly-charged ions (HCI) where the potential energy outweighs the kinetic energy. When a HCI approaches a solid surface it is neutralized again by regaining its missing  $q$  electrons and the potential energy is available for various inelastic processes. The potential energy is deposited within a small surface area (typically  $1 \text{ nm}^2$ ) and a short time (typically about 100 fs) leading to nonlinear excitations [30]. Exotic phenomena like the formation of 'hollow

atoms' [45, 46, 47, 48] and eventually the sputtering of target atoms [49] can take place. For conducting targets only physical sputtering is observed resulting from momentum transfer. For insulating or semiconducting surfaces however the charge mobility within the solid is much smaller and the potential energy introduced by the projectile can be converted into atomic motion and thereby cause sputtering. Since the ejection of these target atoms and ions results from the potential energy of the incoming projectile, this form of sputtering is termed 'potential sputtering' [50, 51]. A more detailed description of potential sputtering can be found in reference [30].

## 2.6 Chemical sputtering

If a target is bombarded with chemically reactive species, chemical effects have to be taken into account and two converse effects can occur [27]. On the one hand, an increase in the sputtering yield can be observed due to the fact that chemical reactions between projectile and target may form more loosely bound species which are more easily sputtered. This process is usually named chemical sputtering. On the other hand, a decrease in the sputtering yield, as compared to kinetic energy transfer alone, can be noticed if the newly formed compounds are more strongly bound to the target atoms. Especially in sputtering processes at low energies ( $< 100$  eV), close to or even below the threshold energy of physical sputtering, chemical sputtering is considered the dominant erosion process.

The effects of chemical sputtering are noticeable in particular for carbon sputtering by the impact of reactive atoms like hydrogen isotopes. This is another major disadvantage in using carbon in form of CFC as a plasma facing component in fusion devices since it leads to enhanced erosion rates and hence to a reduced lifetimes of these components. Besides, sputtered carbon impurities dilute the plasma and retained tritium especially in co-deposited hydrocarbon layers on less exposed areas of the vessel wall become a major safety concern [52]. Chemical erosion processes depend on various parameters like the target surface temperature, the ion flux, the surface state of the material, and the energy of the incident particles [27].

## 2.7 Computer simulation and fitting

A collision cascade, initialized by the impact of an energetic projectile, is a series of atomic collisions between the incident projectile and target atoms and between target atoms themselves [27]. This series of atomic collisions can be simulated with computer programs. One approach, called Binary Collision Approximation (BCA), describes the sputtering process as a sequence of independent binary collisions between atoms. Another possibility to simulate sputter processes is to follow the time evolution of a N-particle system by solving Newton's equation of motion for the system. This approach is called molecular dynamics simulation. In this work, measured sputtering yields are compared to simulations done with TRIM.SP and TRIDYN, which are both programs based on the BCA.

### TRIM.SP

To study the range of ions in matter, Biersack et al [53] developed the TRIM code - **TR**ansport of **I**ons in **M**atter. An extension of this program TRIM.SP [54] also allows the investigation of sputtering processes of amorphous or polycrystalline materials. In this program the incident projectile and recoils generated in collisions are traced until their energy falls below a certain threshold energy. Target atoms are sputtered if the component of the energy normal to the target surface is larger than the surface binding energy. The program uses binary collision approximation, i.e. ion-atom and atom-atom collisions take place sequentially. The key input parameter for simulation programs calculating sputtering yields is the surface binding energy, which is introduced to create a planar attractive force for atoms trying to leave the solid. Usually this energy is approximated by the heat of sublimation. TRIM.SP is a Monte Carlo program, i.e. collisions are chosen randomly after a given mean free path. In this way amorphous and polycrystalline targets can be simulated. The surface of the solid is assumed to be atomically rough, which is implemented by only allowing collisions below a certain depth. The physical sputtering yields calculated with TRIM.SP are generally in good agreement with experimental data, nevertheless uncertainties remain at low impact energies [55].

## TRIDYN

With increasing ion fluencies, ion implantation in the target can lead to a composition change with depth [27] and the formation of a multicomponent target, at least in the range of the ion implantation depth. This affects the sputtering yield since the implanted atoms modify the collision cascade resulting in preferential sputtering effects. An example of such a dynamic simulation program is TRIDYN which is based on the TRIM.SP program for multicomponent targets. This program was used to determine the influence of nitrogen implantation in the tungsten surface and will therefore briefly be introduced in the following.

Dynamic simulation programs, such as TRIDYN [32, 56] can handle these composition changes in the calculation. The preset total fluence impinging on the surface is simulated by certain amount of pseudoprojectiles. Hence each pseudoprojectile corresponds to a fluence interval. Furthermore the target surface is divided into  $N$  layers of thickness  $\Delta x$ . Each atom that is deposited or removed from a layer of thickness  $\Delta x$  during one fluence interval corresponds to a change of the partial areal density [32]. The fractional composition of each layer is updated after the completion of one fluence step. To avoid unphysical over- or underestimation of the total density, relaxation of the total density is allowed afterwards by modifying the thickness of the layer. Before starting a new fluence step the resulting grid is again converted into an equidistant one with the original increment  $\Delta x$  by interpolation.

## Fit formula

Various fit formulae exist to fit experimental obtained sputtering yields. The most widely used formula to fit sputtering yields was introduced by Bohdansky [57] which is based on the analytical description of sputtering by Sigmund [35]. In this diploma thesis an improved fit formula published by Eckstein and Preuss is used [55]. Their fit aims for a better description of yield data compared to previous formulae, especially in the near threshold region. A detailed description of the improvements compared to previous



## 2 Sputtering

fit formula can be found in their work [55]. The fit formula is given by the following equation

$$Y(E_0) = q s_n^{KrC}(\epsilon) \frac{\left(\frac{E_0}{E_{th}} - 1\right)^\mu}{\lambda + \left(\frac{E_0}{E_{th}} - 1\right)^\mu} \quad (2.11)$$

which uses the KrC screening potential [58] to determine the nuclear stopping power

$$s_n^{KrC}(\epsilon) = \frac{0.5 \ln(1 + 1.2288 \epsilon)}{\epsilon + 0.1728\sqrt{\epsilon} + 0.008\epsilon^{0.1504}} \quad (2.12)$$

with the reduced energy given by

$$\epsilon = E_0 \frac{M_2}{M_1 + M_2} \frac{a_L}{Z_1 Z_2 e^2}. \quad (2.13)$$

$e$  is the elementary charge,  $Z_1$  and  $Z_2$  are the atomic numbers and  $M_1$  and  $M_2$  are the masses of projectile and target atom, respectively. The reduced Lindhard screening length is given by

$$a_L = \left(\frac{9\pi^2}{128}\right)^{1/3} a_B \left(Z_1^{2/3} + Z_2^{2/3}\right)^{-1/2} \quad (2.14)$$

where  $a_B$  is the Bohr radius. The threshold energy  $E_{th}$  and the independent parameters  $q$ ,  $\lambda$  and  $\mu$  are used to fit the formula to experimental obtained data. These fit parameters for various ion-target combinations can be found elsewhere [27].

## 3 Experimental Setup

### 3.1 The quartz crystal microbalance technique

Already in 1959 Sauerbrey proposed using a quartz vibrator as a microbalance for weighing thin layers [59]. He showed that the eigen-frequency of a quartz crystal vibrating in its fundamental thickness shear mode is proportional to its mass. This also holds true for a thin film deposited onto the crystal, as long as the thickness of this film is negligible compared to the thickness of the crystal. By using this principle we are able to measure the net mass removal of this deposited film caused by the impact of incoming particles.

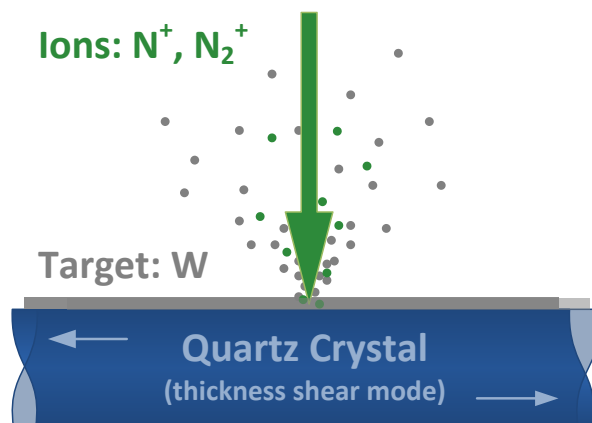


Figure 3.1: Principle of the quartz crystal microbalance technique: The mass of the crystal defines the eigen-frequency of the thickness-shear-mode. This also holds true for a thin film of target material (W) deposited onto the crystal. Mass changes, due to the impact of incoming particles, are proportional to a frequency change, which can be measured with high accuracy.

### 3 Experimental Setup

The correlation of the total mass change of the quartz crystal to a change in its oscillation frequency is known as the Sauerbrey equation given by

$$\frac{\Delta m}{m} = -\frac{\Delta f}{f} \quad (3.1)$$

Due to this correlation, a quartz crystal can be used as a mass-sensitive device of very high accuracy, so-called Quartz Crystal Microbalance (QCM), as the frequency measurement can be done with high precision. However, this method is only sensitive to total mass changes. Effects causing an increase in the mass ( $\Delta m > 0$ ) cannot be disentangled from other effects that remove mass from the crystal ( $\Delta m < 0$ ).

As we are more interested in the total sputtering yield than in the mass change, i.e. the removed number of target atoms per projectile, we also have to determine the number of incoming ions. This is done by measuring the ion current  $I$  over a time  $\Delta t$ . The number of incoming ions is then given by the current divided by the charge state  $q$  times the elementary charge  $e_0$ .

$$N = \frac{I \Delta t}{q e_0} \quad (3.2)$$

The total sputtering yield of a thin film deposited onto the crystal in atomic mass units (amu) per incident ion can then be determined by simply dividing the mass change by the number of incident ions

$$Y[amu/ion] = -\frac{\Delta m/m_u}{N} = \frac{q e_0}{m_u f} \frac{m}{I} \frac{\Delta f}{\Delta t} = \frac{q e_0}{m_u f} \frac{\rho d}{I/A} \frac{\Delta f}{\Delta t} \quad (3.3)$$

with  $m_u$  being the conversion factor between SI-units and atomic mass units (amu). The ion current density  $I/A$  from the above expression can be determined by simply measuring the current with a Faraday Cup (FC), connected to a pico-amperemeter. However, in this respect it is crucial, that the whole active area of the quartz crystal is covered with a homogeneous, constant beam spot and that the current density remains stable throughout the whole experiment. By monitoring the eigen-frequency of the crystal during ion irradiation, the slope of the frequency per unit time  $\Delta f/\Delta t$  can be determined. The constants necessary to evaluate the sputtering yield with equation 3.3 are given below:

### 3 *Experimental Setup*

---

elementary charge	$e_0$	$1.60217653 \cdot 10^{-19}$ C
atomic mass unit	$m_u$	$1.66053886 \cdot 10^{-27}$ kg
mass density of the crystal	$\rho$	2649 kg/m <sup>3</sup>
thickness of the crystal	$d$	$0.302 \cdot 10^{-3}$ m
area of the Faraday cup	$A$	$1.13097 \cdot 10^{-6}$ m <sup>2</sup>
eigen-frequency of the crystal	$f$	5.998 MHz

## The quartz crystal

The QCM system at TU Wien [60, 61] that is used for sputtering yield measurements has been designed to perform in situ measurements of ion surface collisions with high accuracy. Golczewski et al [62, 63] showed that this setup is capable of detecting mass-changes as small as  $10^{-5}$   $\mu\text{g/s}$ , which correspond to a removal of only  $10^{-4}$  tungsten monolayers/s. The quartz crystal we use, is a plano-convex disk with a resonance frequency of about 6 MHz and a diameter of 13.95 mm available from KVG Quartz Crystal Technology GmbH, Germany. In general crystals are cut at different orientations from the bar of quartz in order to realize specific characteristics for different applications. Instead of the common AT cut we use a stress compensated (SC) cut crystal, which has the advantage of being more insensitive to radial stress that can arise from non-uniform mass removal of the target film during ion bombardment. Gold electrodes are deposited on each side of the crystal to ensure good electrical contact to the oscillator circuit.

On the beam-facing side of the crystal an additional layer of tungsten has been added by magnetron sputter deposition at the Institute of Solid State Physics at TU Wien by Prof. Eisenmenger-Sittner. This polycrystalline tungsten film has a thickness of about 500 nm. By using polycrystalline films we can avoid sputter effects resulting from the orientation of the crystalline structure of the target.

## Sample holder

The quartz crystal is mounted on a sample holder within an Ultra High Vacuum (UHV) chamber connected to the ion source. Figure 3.2 shows an exploded view of the sample holder. A thermocoax heating unit (colored in yellow) is fixed between two stainless steel

### 3 *Experimental Setup*

plates at the frontside of the holder. The quartz crystal (colored in red), coated with the gold electrodes and the tungsten film on the beam-facing side, is clamped between these plates with a thin golden ring at the front and a tungsten spring (colored in blue) at the backside. This provides good electrical contact and reduces mechanical stress in the crystal caused from the mounting. The golden ring connects the front electrode of the crystal with the sample holder which is kept at ground potential. The electrode on the backside is connected to the QCM electronics via the tungsten spring and the screw for the mounting of this spring. Ceramic split bushes (colored in green) isolate this screws from the other components of the sample holder, which are on ground potential. The FC is designed as cup drilled into a screw, which is situated behind an entrance aperture with a diameter of 0.6 mm. This aperture is located 17 mm above the centre of the crystal. The screw of the FC is again electrically isolated from the other components of the sample holder via ceramic split bushes.

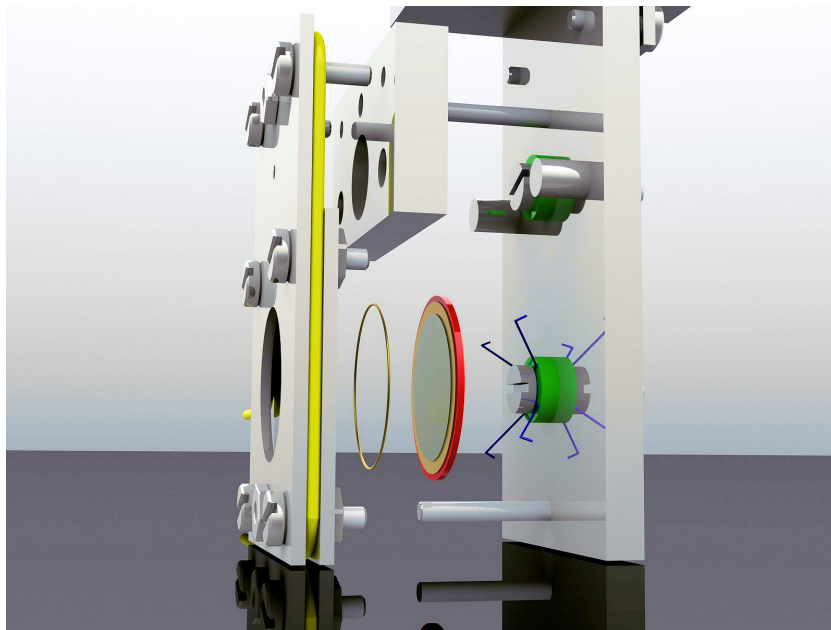


Figure 3.2: Sample holder with the quartz crystal (colored in red), the heating (colored in yellow) and the tungsten spring (colored in blue)

As part of the modernization of the vacuum system (cf. section 3.3) we also exchanged the manually movable x-y-z- $\varphi$  manipulator by a manipulator driven by stepper motors. Since the new manipulator has a nominal diameter of 150 we also had to replace the CF 100 double cross supporting the manipulator by a CF 150 double cross. Since the dimensions of the vacuum chamber and the manipulator changed that much, it was

### 3 *Experimental Setup*

necessary to redesign the sample holder of the quartz crystal in order to maintain full functionality. Before the reconstruction of the vacuum system we removed the whole manipulator from the vacuum chamber, whenever we had to exchange the crystal in the sample holder. This is not possible anymore with the new manipulator. The new sample holder, shown in figure 3.3, is divided into two parts: the upper part is the link to the manipulator and stays in the chamber at all time. The lower part (coloured in green), which holds the quartz crystal, is attached to the upper part via a dovetail and can be fixed with two screws on top (coloured in red). For maintenance or the exchange of a crystal, the lower part can now easily be removed from the chamber just by loosening this two screws. All electrical connections, like the cable to the quartz crystal or to the FC, are now equipped with UHV adequate push connectors for facile plugging and unplugging.

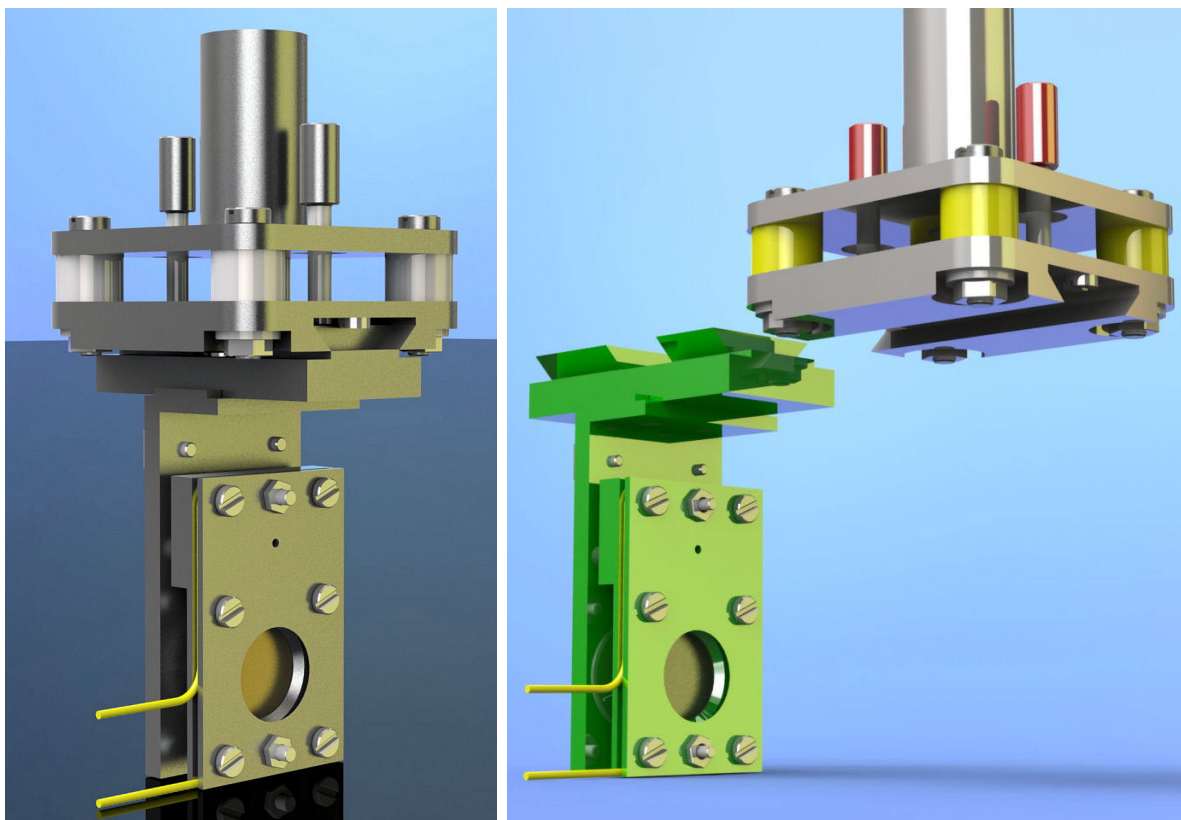


Figure 3.3: The QCM holder is now divided into two parts: the upper part, which is the connection to the UHV manipulator, remains in the vacuum chamber all the time, whereas the lower part (coloured in green) can be dismantled by simply loosening the red coloured screws on the top. All electrical connections, except the thermocouple, are now implemented using push connectors. This allows us to easily plug and unplug all wires within the vacuum chamber.

## Temperature control

Temperature fluctuations have a relatively high influence on the eigen-frequency of the quartz crystal and can be considered as one of the main error sources in the determination of the total sputtering yield with QCMs. By monitoring the eigen-frequency, as a function of the temperature, a minimum, usually between 185°C and 200°C, of the frequency can be observed (cf. figure 3.4, here the minimum in the frequency is at 190°C). At this temperature the frequency of the crystal is most insensitive to temperature fluctuations and therefore the microbalance is operated at this temperature. The heating of the quartz crystal is done with a thermocoax heating distributed by Philips (type TE128319) which is clamped between two stainless steel plates as already mentioned in the previous section. The temperature is measured by a thermocouple clamped to the front-plate. By providing a good thermal contact between the front plates and keeping the temperature measurement in close vicinity of the crystal, we can assume that the measured temperature is equal to the temperature of the crystal. The power supply unit of the heating is regulated by a PID controller with the measured temperature serving as input signal. In this way the temperature of the crystal can be kept constant at the minimum of its frequency over temperature curve within an accuracy of  $\pm 0.1^\circ\text{C}$  even during ion bombardment.

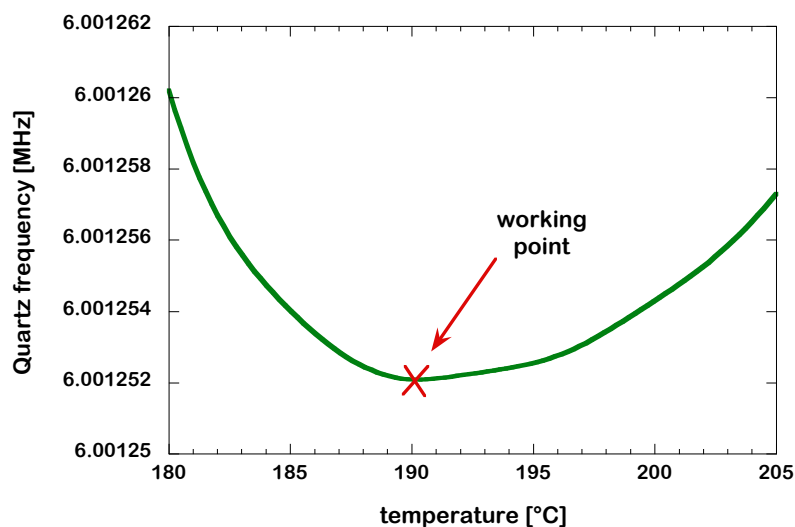


Figure 3.4: The frequency of a quartz crystal depending on the temperature shows a minimum usually in the range between 185°C and 200°C. In the case shown above, the minimum lies at about 190°C

## QCM electronics

The primary tasks of the QCM electronics is to drive the quartz crystal at its eigen-frequency and to measure this frequency with a precision of a few mHz [61]. The electronics is the key element of the microbalance setup to ensure extremely high accuracy and sensitivity.

The equivalent circuit of a quartz crystal is a Butterworth - van Dyke circuit (cf fig 3.5) driven at its fundamental oscillation frequency in series resonance. The geometry of the crystal is equivalent to that of a parallel-plate capacitor. So if the frequency of the applied alternating voltage is distinct from the resonance frequency of the crystal, it will behave like a capacitor. In this case the quartz is equivalent to the capacitance  $C_0$  given by its dielectric constant, the area of its electrodes and its thickness. If the excitation frequency of the applied voltage is similar to the eigen-frequency of the crystal the atoms in the crystal start to oscillate. This mechanical oscillations are electrically equivalent to a resonance circuit composed of  $L_q$ ,  $C_q$  and  $R_q$  in parallel to the capacitance  $C_0$ . The phase shift between the excitation frequency and the oscillation frequency can be used to measure the oscillation frequency. If the excitation frequency is smaller than the resonance frequency the phase shift is negative and vice versa. Therefore, the phase difference between the excitation voltage and the oscillation frequency is used to control the oscillator's frequency as in a phase-locked loop.

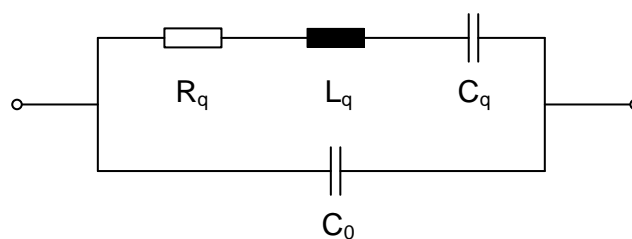


Figure 3.5: Butterworth - van Dyke circuit: This is the equivalent circuit of the quartz crystal.

The electrical wiring between the electronics and the quartz crystal adds an additional, non-negligible capacitance parallel to  $C_0$ . To compensate for these capacitances, two branches of electrical wiring are used, which are identical except that only one branch is



connected to the quartz crystal. In this way it can be assured that both branches add the same parallel capacitance to the circuit. The signal of the compensation branch can then be used to correct the signal from the quartz crystal in a differential amplifier [61, 64].

## 3.2 Ion Source and beam alignment

In the following section, a short overview of the ion source and the ion optics system at the Institute of Applied Physics (TU Wien) will be given.

### Ion Source

The Electron Cyclotron Resonance (ECR) ion source, lovingly nicknamed SOPHIE (**S**ource for **P**roduction of **H**ighly charged **I**ons using **E**lectron cyclotron resonance) at the Institute of Applied Physics at TU Wien is capable of producing singly and multiply charged ions at extraction voltages up to 6 kV and with charge states up to  $\text{Ar}^{11+}$  [65, 66]. The ions are generated by step-by-step ionization induced by electrons within a plasma chamber. The magnetic field for the confinement of the plasma is provided by four permanent magnet rings and a Halbach-type hexapole. To optimize the extraction of differently charged ions, the whole permanent magnet configuration can be shifted along the plasma chamber axis.

In an electron cyclotron resonance ion source microwave radiation is used to resonantly heat the electrons in the plasma. This leads to high electron temperatures in the plasma chamber capable of producing highly charged ions. The microwaves are transmitted into the chamber through a Polytetrafluoroethylene (PTFE) window, which isolates the waveguide system from the main chamber. Therefore the waveguide and the microwave power supply system can be kept at ground potential. In the vacuum chamber, the waveguide changes from a rectangular to cylindrical geometry. This part of the microwave guiding system can be biased negatively with respect to the plasma potential. By this the plasma potential is increased by reflecting a sufficient amount of electrons back to the plasma and the ion charge state distribution can be improved [67]. A solid



Figure 3.6: Computer model of the ion source SOPHIE at TU Wien used to produce the ions for the sputtering yield measurements

state amplifier is used to amplify the microwaves after they are generated in a thin film oscillator in the range between 12.75 GHz and 14.5 GHz.

The source is equipped with two gas inlet valves, which allow to use a mixture of gases in the plasma chamber. This is especially beneficial for the production of highly charged ions. The valves are isolated from the chamber and can therefore be held at ground potential. As the whole ECR ion source is computer controlled, all operating parameters can be monitored by a LabVIEW based program [68].

The extraction of the ions from the plasma is done by using a triode 'accel-decel' extraction system [65]. The ion beam is accelerated from the positive plasma potential to the ground electrode. An additional suppressor electrode, between the plasma and the ground electrode, compensates the space charge of the extracted ions and allows to extract intense, well collimated ion beams. With the 'accel-decel' extraction system we are able to extract ions from the plasma with extraction voltages up to 6 kV.

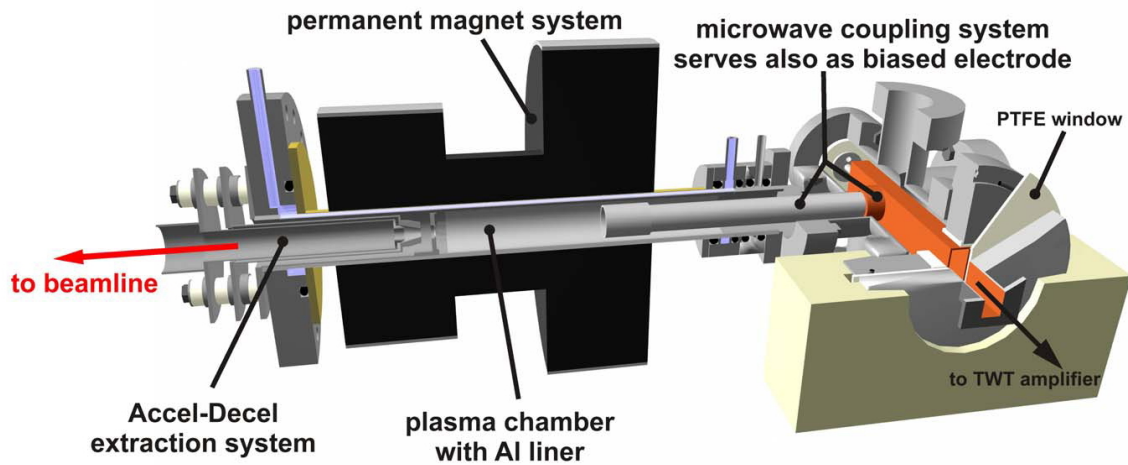


Figure 3.7: A sectional view of the ion source showing the microwave system, the plasma chamber surrounded by the permanent magnets and the extraction system. Picture taken from [65]

## Ion optics

The extracted ions are focussed by a pair of magnetic quadropoles with perpendicular focussing planes and mass over charge selected in a subsequent sector magnet (cf figure 3.8). A FC mounted on a pneumatic manipulator, located between the sector magnet and the beamline entry, can be used for measuring the spectra of the extracted ions. The QCM beamline houses two sets of deflection plates and an electrostatic lens system which are used to deflect and focus the beam onto the target. Apertures are used to collimate the beam and a set of scanning plates to scan the beam across the whole target surface.

A more detailed drawing of the ion optics system within the beamline is given in figure 3.9. Two sets of deflection plates (cf. (a) and (c) in fig. 3.9) are sufficient to deflect the incoming ion beam through the apertures ((b) and (d)) and onto the FC ((g)) on the sample holder. By applying an appropriate voltage to lens two, while holding all other lenses at ground potential, we are able to focus the ion beam and to increase the measured ion current in the FC. Inhomogeneous mass removal during the ion bombardment can impose mechanical stress onto the quartz crystal. To avoid this the ion beam is scanned with a set of scanning plates ((f)) across an area at least the size of the active area of the crystal. This is done by applying a triangle signal on each pair of scanning

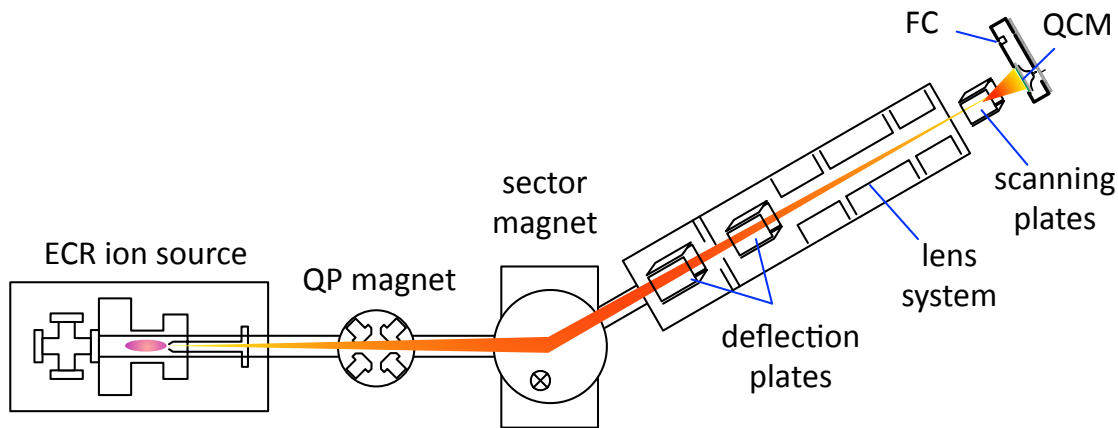


Figure 3.8: Schematic overview of the experimental setup at the Institute of Applied Physics at TU Wien

plates with a frequency of 52 Hz on one spatial direction and 1.6 kHz on the other. In this way it is assured, that no pattern is scanned onto the crystal surface. The ion current density, needed to determine the sputtering yield (cf. equation 3.3), is measured thereafter with the FC and the sample holder is subsequently lifted to the quartz crystal position with the manipulator.

The profile of the scanned ion beam is not of perfect rectangular shape but rather follows a Gaussian distribution. Therefore the amplitude of the scanning voltage is tuned to a value where the active area of the quartz crystal lies within the more or less constant centre of the Gaussian curve. Attention has to be paid to the size of the beam spot. If the active area of the quartz crystal is not completely covered by the scanned ion beam, equation 3.3 (in this simple form) is not valid. By changing the diameter of the beam spot for a fixed target ion combination, a critical beam diameter of about 6 mm could be determined [69]. Thus measurements have been conducted with a beam spot diameter greater than the critical beam diameter in order to guarantee that the irradiated area always exceeds the active, vibrating and hence mass-sensitive area of the crystal.

To measure the total sputtering yield as a function of to the energy of the ions, the energy of the ions has to be varied. Since the kinetic energy of the projectiles is equal to the charge state times the extraction voltage this can be done by either changing the extraction voltage of the ion source or switching to a differently charged ion with the sector magnet, at fixed extraction voltage. In the latter case, it must be ensured

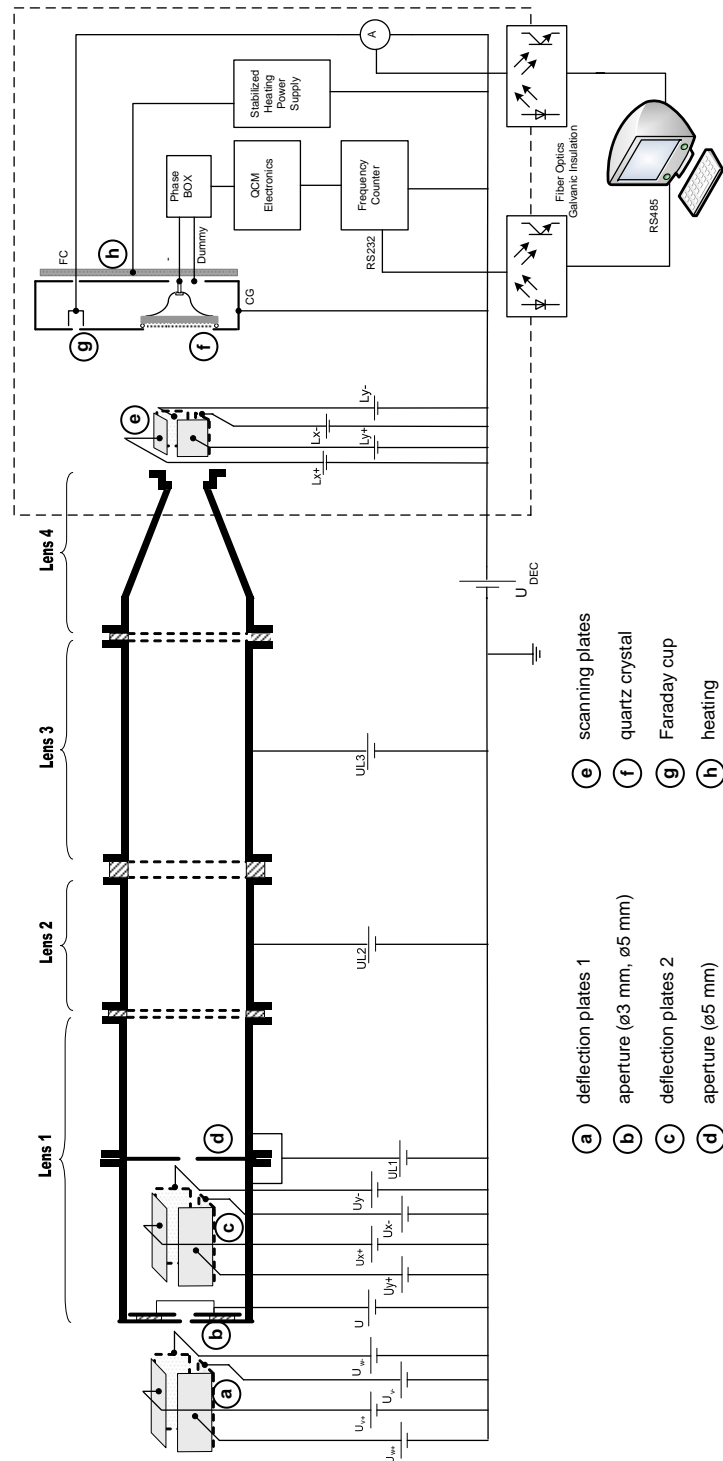


Figure 3.9: QCM block diagram



Figure 3.10: Computer model of the lens system used to focus and decelerate the ions when needed.

that the sputtering yield does not depend on the charge state of the ion. Below about 500 V extraction voltage, the performance of the extraction system of the ion source is not sufficient and the resulting beam intensity too low to perform measurements. In order to conduct measurements at energies below  $q \cdot 500$  eV, the impact energy of the projectiles can also be varied by decelerating them before they impinge on the surface. This is done by applying a positive voltage to the target at a fixed extraction energy. In order to do that, the voltage has to be applied not only to the quartz crystal and the sample holder, but also to the scanning plates, to lens four and to the heating to avoid accelerating the ions from the deceleration lens towards grounded parts and thereby distorting the beam. For this purpose several electronic devices can be operated at high voltage and are therefore situated in a high voltage cage: the QCM driving electronics, the stabilized heating power supply, the frequency counter, the pico-amperemeter and the supply unit of the scanning plates (cf. figure 3.9). To avoid operating the computer also at high voltage, the data from the frequency counter is transferred to the computer as an optical signal via a fibre cable for galvanic isolation.

## Measuring procedure

The typical procedure for measuring sputtering yields with the QCM is outlined below. As already mentioned in section 3.1 by using a quartz crystal, the sputtering yield can be measured by determining the slope of the frequency change during ion bombardment. An important point in this respect is the correction of frequency drifts originating from instabilities in the temperature or from the oscillator circuit of the QCM electronics. For this reason these frequency drifts are monitored before and after irradiating the quartz crystal and can be subtracted from the measured frequency slope afterwards. Therefore all measurements are divided into three phases: In phase one and three, the ion beam is blocked by the UHV shutter and the frequency drift, primarily due to the thermal instabilities, is monitored. In phase two, the shutter is opened and the quartz crystal is irradiated with the ion beam. A LABVIEW program records the frequency from the frequency counter and fits the three phases of the measurement linearly. In this way the frequency slope, as observed during ion bombardment, can be automatically corrected by the program. If the sputtering yield was not constant over time and cannot be fitted with one linear fit, the measurement must be evaluated manually afterwards. For this reason the program also produces an output file with the frequency change as a function of time.

The procedure to measure the sputtering yield with the QCM is given in the following:

- Setting up the ion source
- Selection and optimization of the desired ion: This can be done by measuring the ion current in the Faraday cup at the beamline entrance and tuning the current of the quadrupole and the sector magnet.
- Opening the shutter of the beamline and focusing the beam onto the Faraday cup of the sample holder
- Scanning the focused beam with the scanning plates to a size that covers the whole active area of the quartz
- Determination of the beam profile by moving the Faraday cup along two axes with the UHV manipulator.

- Closing the shutter and lifting the sample holder so that the centre of the crystal is positioned at the centre of the beam spot.
- Waiting for the quartz frequency to stabilize, which is necessary after moving the sample holder
- Starting the measurement with a beam off phase, followed by an ion irradiation phase by opening the shutter and a second beam off phase with the shutter closed again. Each phase lasts several minutes.
- Evaluation of the linear fit for the frequency change in each phase, correction of the gradient of the beam on phase by the average of the two beam off phases and determination of the sputtering yield by using equation 3.3

### **Accuracy estimation of the measurements**

The two key parameters to evaluate the sputtering yield with a QCM are the slope of the frequency change during irradiation and the impinging ion current density. Both are sources for errors and have to be determined carefully. Nevertheless when working with an ECR ion source some fluctuations in the ion current, arising from plasma instabilities, cannot be eliminated and have to be taken into account. Therefore after determining the beam profile only three measurements in a row have been conducted and then the ion current was controlled again. Thereby it was possible to correct the evaluation of the sputtering yield afterwards by assuming a linear change of the ion current.

The correct determination of the frequency slope during ion irradiation can become problematic when the thermal drifts of the quartz crystal are in the order of the frequency change resulting from the mass change due to ion irradiation. Thus changes in the thermal drift are then sources for significant errors. This is especially the case for low ion current densities in the low energy regime, where it is difficult to extract a sufficient amount of ions from the ECR ion source.

The smaller the mass changes, that one wants to detect, the higher is the frequency stability that is required. Since with our measurements we want to investigate mass changes in the order of some fractions of monolayers per minute the frequency stability



has to be in the range of a few mHz/min for both, the quartz crystal and the oscillator circuit. By investigating the frequency changes without ion irradiation, the frequency drift of the setup was determined to be about 2 mHz/min with thermal noise of approximately 3 mHz [64]. From a series of measurements with small frequency changes, due to low ion currents, it could be concluded that this QCM setup is limited to experiments where the product of total mass change times ion current density is greater than  $0.2 \text{ amu/ion} \cdot \mu\text{A/cm}^2$  [61]. This corresponds to mass changes of approximately  $10^{-5} \mu\text{g/s}$  or  $10^{-4}$  tungsten monolayers per second.

### 3.3 Vacuum system

In the course of this diploma thesis the whole vacuum system of the ion source facility and therefore also of the QCM beamline was renewed. Before this renovation, we used a rotary pump for the prevacuum and two turbo molecular pumps for each beamline, whereas the UHV chambers connected to the turbo pumps, were separated by small apertures. With this differentially pumped setup we reached a vacuum pressure, in the chamber of the experiment, in the order  $10^{-8}$  mbar to  $10^{-9}$  mbar.

The main difference now is that we use two ion pumps per beamline instead of the two turbo molecular pumps to generate the UHV conditions. This gives us the possibility to conduct our experiments in an completely vibrational free environment. For further decreasing the vacuum pressure inside the experimental vacuum chamber, one of these ion pumps is equipped with an additional Titanium Sublimation Pump (TSP). With this vacuum pump configuration we are able to reach a vacuum pressure of some  $10^{-10}$  mbar, i.e. more than one order of magnitude lower than before.

To improve cleanliness inside the vacuum chambers, especially to remove oil dispersed in the air, the rotary pumps for the prevacuum pumping have been replaced by a dry pump system. The prevacuum pumping is now done with one central oil-free scroll pump produced by Varian with a pumping speed of 7 l/s.

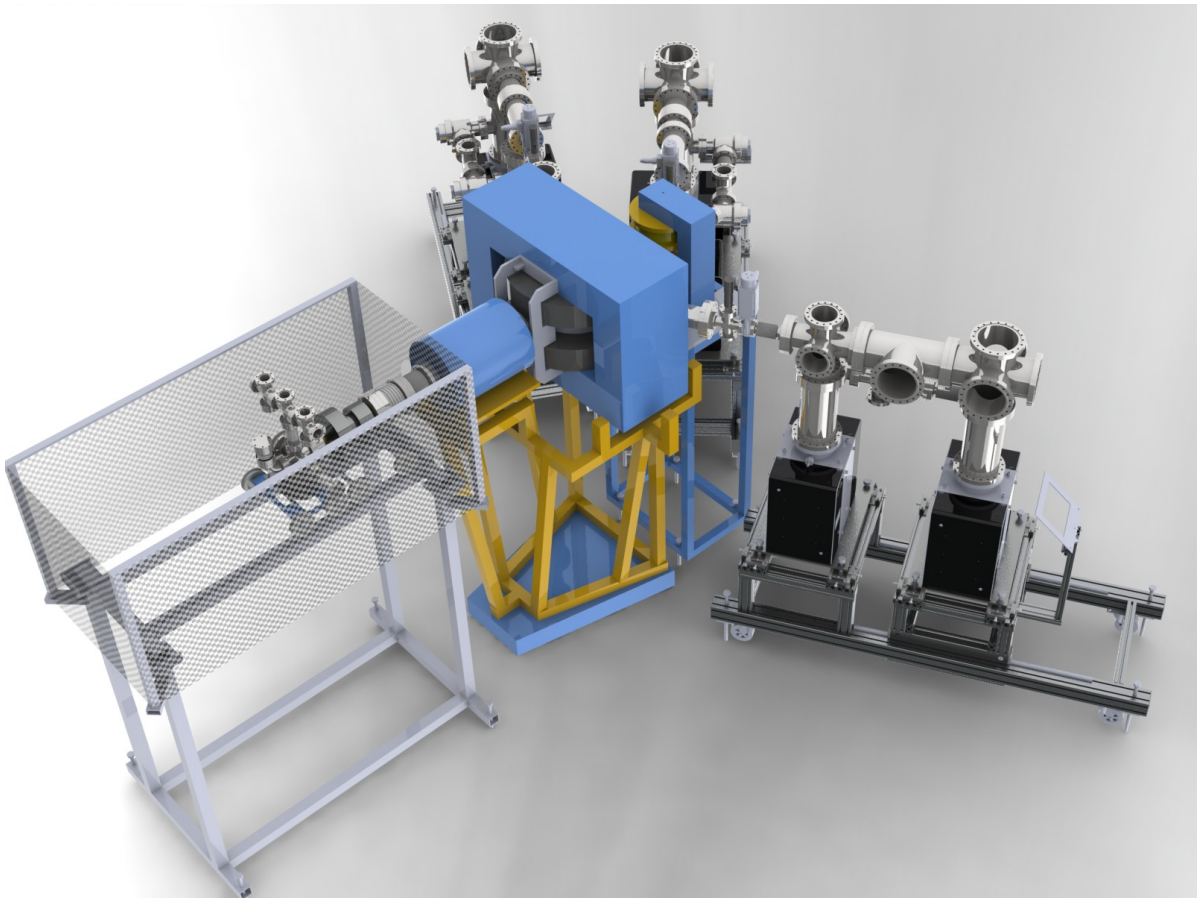


Figure 3.11: Computer model of the whole ion source facility at the Institute of Applied Physics at TU Wien showing the ion source, the quadrupole magnet, the two sector magnets and the three beamlines.

### 3.3.1 Operation of ion pumps

Ion pumps are widely used in scientific apparatuses such as particle accelerators, mass spectrometers or particle beam devices. As already mentioned above, they provide a vibrational free, clean and economic way of achieving UHV. Each ion pump is built up of several pumping elements, which consist of anode tubes and cathode plates. The amount of pumping elements determines the pumping speed. This pumping elements are surrounded by a permanent magnet structure [70].

After roughly pumping the ion pump with an auxiliary pump to a pressure of at least  $10^{-4}$  mbar (for the lifetime of the ion pump it is better to pump to  $10^{-6}$  mbar or even lower) the pump can be started by applying high voltage between the anode tubes

and the cathode plate. Once the high voltage has been applied a cloud of electrons forms within the anode structure. These accelerated electrons are now able to ionize gas molecules and atoms by electron impact ionization. The magnetic field of the permanent magnets force the electrons to travel in a circular, or in general helical, pattern. This increases the distance an electron will travel and therefore increases the chance of ionizing gas molecules. The positively charged gas molecules are accelerated towards the cathode plate of the pumping element. Upon impact these ions are chemically bound provided that the gas is chemically reactive. The relatively high impact energy of the ions also causes sputter processes on the cathode surface. Therefore cathode material is spread throughout the pumping element and subsequently fresh cathode material is constantly available at the surface. Noble gases such as argon and xenon are less reactive and can therefore not be chemically bond chemically to the cathode material. With triode pumping elements noble gases can be pumped too, as the ions impinge at glancing angles onto the cathode. This directs most of the incoming ions further towards the vacuum chamber wall of the ion pump [70].

Since most of our experiments are conducted with noble gas ions we decided to use triode pumping elements even though they are more expensive and electrically more unstable. The ion pumps are equipped with eight pumping elements giving a pumping speed of 480 l/s and were produced by Gamma Vacuum.

### 3.3.2 Vacuum system setup

As the ion pumps are quite massive (about 105 kg per ion pump) we also needed to build a new support structure for all three beamlines. Besides stability the main criterion in the design of these support structures was the ability to align the beamlines with the adjacent vacuum vessels of the sector magnets. To facilitate the maintenance of the experiments and also of the ion optics system we furthermore wanted to be able to separate the experimental vacuum chamber from the second chamber needed for the differential pumping stage. All these requirements could be met by designing a support structure based on the MB Building Kit System from ITEM [71]. This system also allows us to easily modify and add support structures if needed. Figure 3.12 shows the QCM beamline with the support structure. Both ion pumps rest on plates made of Teflon, which has a very low friction coefficient. Therefore the whole setup can be

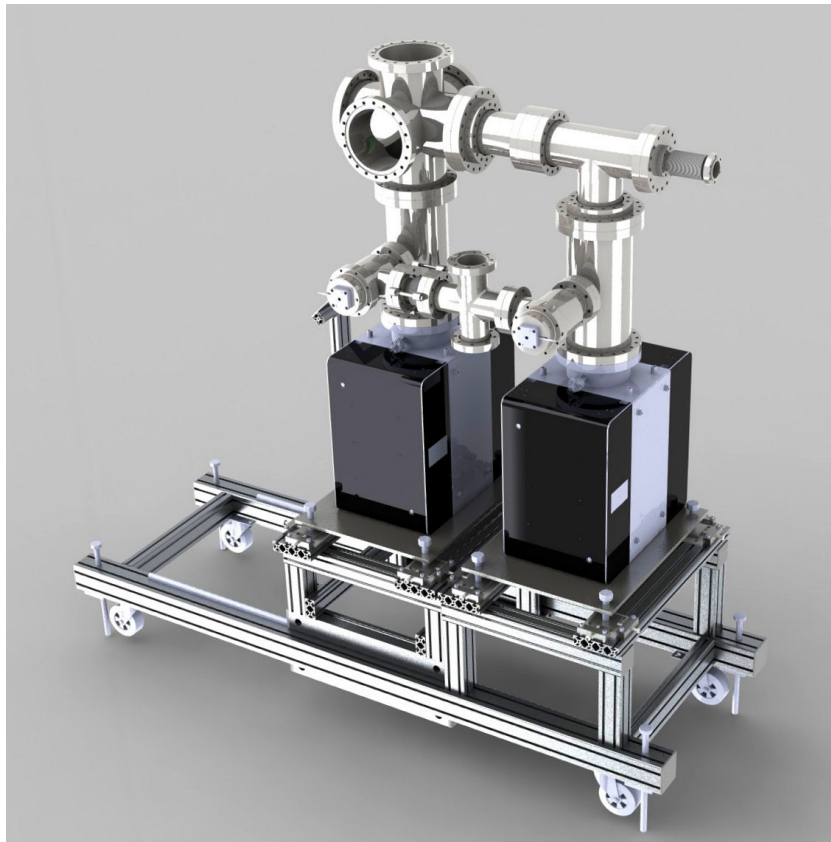


Figure 3.12: Model of the vacuum system of one beamline showing the two ion pumps produced by Gamma Vacuum

shifted, for the alignment of the beamline, with a reasonable amount of effort and can be blocked afterwards. The ion pump, which also houses the TSP, is placed on a roller carriage and can easily be shifted backwards so that the UHV chambers can be separated for maintenance reasons. To move the whole setup if needed, we added four transport wheels on the bottom of the main structure.

The vacuum plan of the whole ion source facility [72] can be found on page 48. The vacuum system is coloured in black, gas lines are drawn in blue and pressured air lines in turquoise. The facility consists of the ion source, a quadrupole magnet, two sector magnets and three beamlines housing different experiments. In the course of the refurbishment of the vacuum system, the three beamlines were adapted and are now equally equipped. In the following the setup of one of these beamlines (beamline 1) is described. A detailed drawing of the vacuum plan for beamline 1 is shown in figure 3.13.

The vacuum vessel containing the experiment (VV-1-2) is separated from the sector

### 3 Experimental Setup

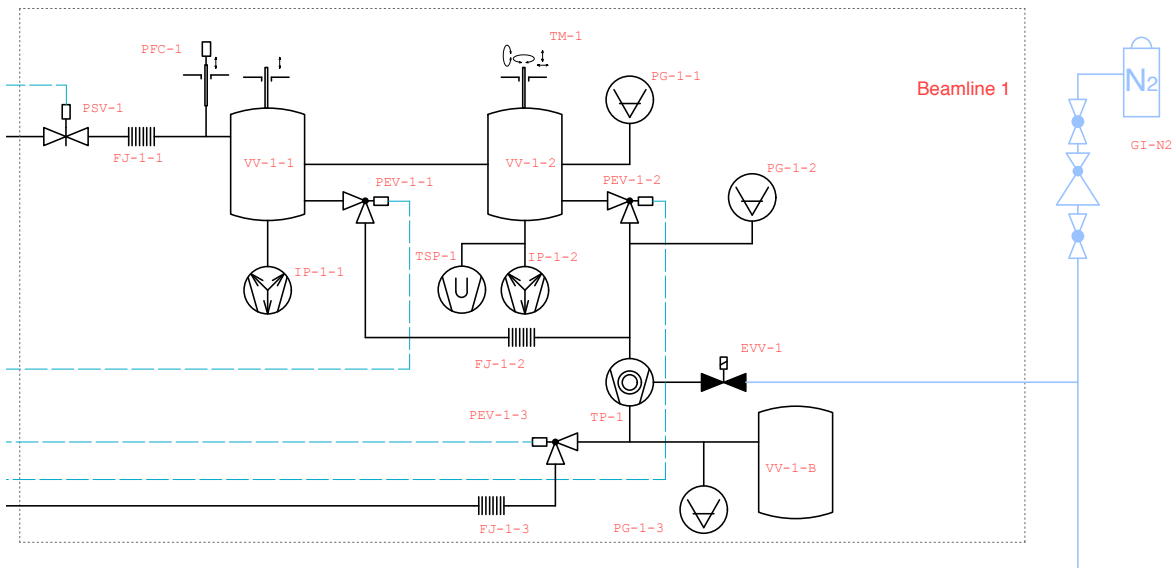


Figure 3.13: Plan of the vacuum system for one beamline.

magnet by another vacuum vessel (VV-1-1), which is needed for the differential pumping stage. The two vacuum chambers are separated by small apertures. By this the vacuum pressure is lowered from typically  $10^{-7}$  mbar in the sector magnet to  $10^{-10}$  mbar in the experimental chamber. Each vacuum chamber is located above an ion pump labelled with IP-1-1 and IP-1-2. The x-y-z- $\varphi$  manipulator (denoted by TM-1) mounted on top of the collision chamber (VV-1-2), is used for positioning the target holder with respect to the ion beam. Between the ion pumps and the vacuum chambers of the beamline, reducer crosses and T-pieces have been installed to build up a bypass system. A turbo molecular pump (TP-1) with a pumping speed of about 67 l/s for  $N_2$  is connected to the main vacuum chambers via this bypass. This enables, on the one hand, the rough pumping of the whole system, which is needed prior to starting the ion pumps. On the other hand, the turbo pump can support the ion pumps during high gas load operation scenarios.

A Bayard-Alpert gauge (PG-1-1) measures the vacuum pressure within the main chamber. The vacuum pressure of the bypass is monitored with a combined Pirani / cold cathode ionization gauge (PG-1-2), which is mounted just above the turbo molecular pump. An UHV shutter (PSV-1) separates the beamline from the adjacent sector magnet and can be used to switch the beam on and off. The FC mounted on a pneumatic manipulator (PFC-1) can be used to measure the ion beam current entering the beamline

### 3 *Experimental Setup*

---

and thereby optimizing the settings for the sector magnet as well as for the quadrupole magnet.

The prevacuum system of each beam line consist of a buffer vessel (VV-1-B) and a prevacuum pressure gauge (PG-1-3) and is connected to the turbo pump. The prevacuum pumping for the whole facility is now done with one central prevacuum pump. This prevacuum pump is separated from the prevacuum system of the beamline by an angle valve (PEV-1-3). Given that, in the UHV regime, the gas load is very low and the turbo molecular pump can be operated at prevacuum pressure up to 5mbar, there is no need to pump the prevacuum of each beamline at all time. A Programmable Logic Controller (PLC) monitors the prevacuum pressure of each beamline and pumps it, by starting the pump and opening the angel valve PEV-1-3, only if needed.

We renewed the turbo molecular pumps and pressure gauges of the sector magnet and the ion source as well. The turbo pump of the ion source (TP-S on page 48) is of the same type as the turbo pumps installed in the bypass of the beamlines. The pumping of the sector magnets is done with a slightly bigger turbo pump (labelled TP-M) with a pumping speed of about 260 l/s for N<sub>2</sub>. It is located next to one of the sector magnets. To decrease the amount of hydrogen and water inside the vacuum chambers we now use clean, dry nitrogen instead of air for the venting of the chambers. For this reason the venting valves of all turbo pumps are connected to the nitrogen wall outlet of the laboratory (GI-N2 in figure 3.13 and on page 48).

As already indicated above, the control of the vacuum components, which was formerly distributed over the whole facility, is now done at one central point with a PLC. In this way we are also able to operate the vacuum system in a full automatic mode.

Figure 3.14 shows a plan of the whole vacuum setup after the renewal.

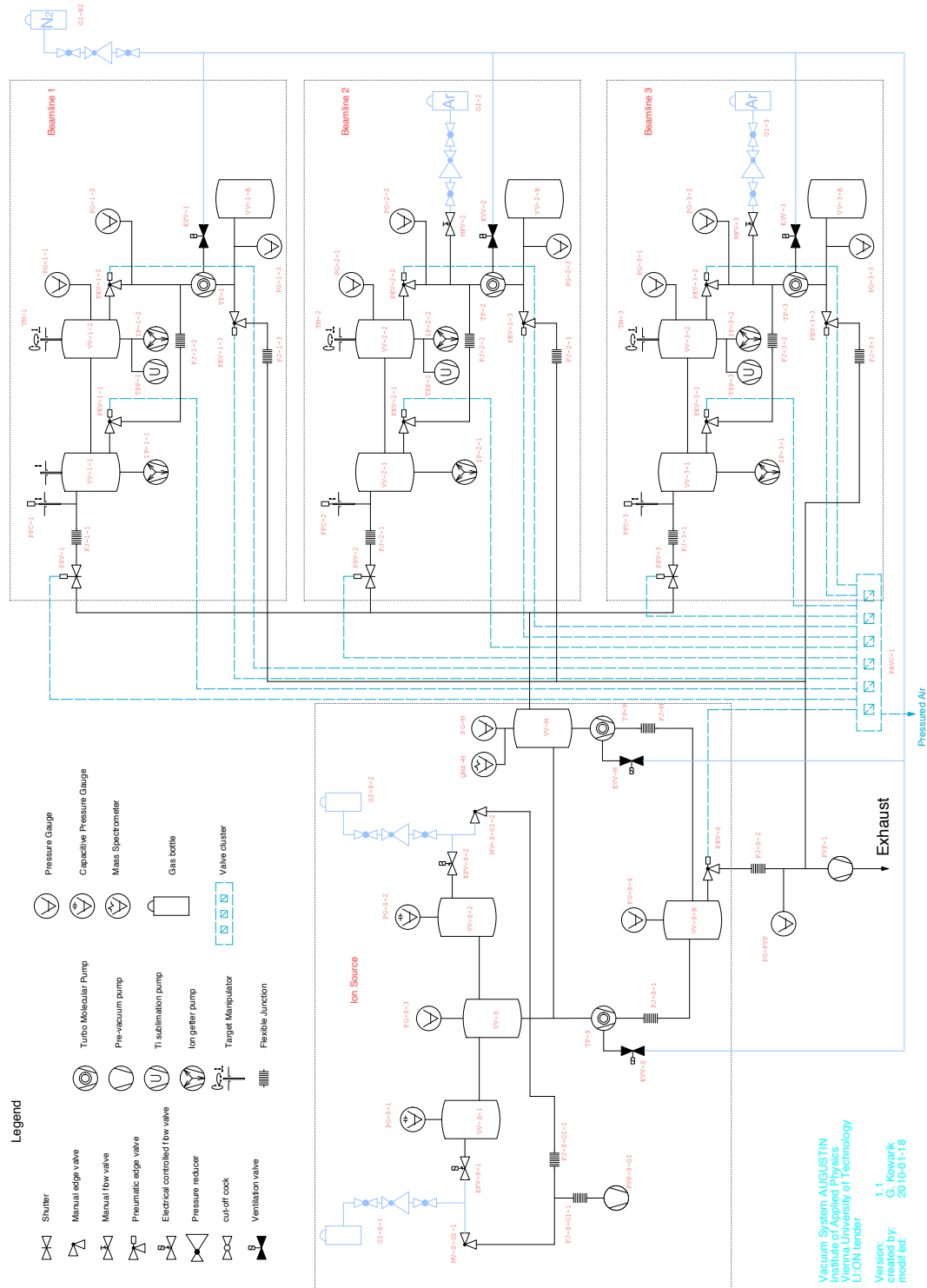


Figure 3.14: Plan of the whole vacuum system taken from [72]

## 4 Results and discussion

### 4.1 Beam profile

After setting up the ion source and focusing the ion beam onto the FC of the sample holder, the ion beam was scanned across the surface of the crystal to guarantee homogeneous irradiation (cf. page 37). By covering the whole active area of the crystal with a homogeneous ion beam flux, the current density can be used to evaluate the sputtering yield. For this reason the scanning voltage was increased to a level, where the beam plateau of the ion beam profile is at least of the size of the active area of the crystal (diameter of about 6 mm, see also page 37).

The shape and size of the beam spot was then determined by stepwise moving the FC with a step size of 1 mm along two axes and measuring the current with the picoamperemeter. A typical beam profile, obtained in this way, is shown in figure 4.1. The active area of the crystal is symbolized as a green circle with a diameter of about 6 mm. The current density, which is needed to evaluate the sputtering yield (cf. equation 3.3) is then calculated as the mean of all measured values, within the active area, divided by the area of the FC. The mean value and standard deviation of the shown beam profile is  $58 \pm 4$  pA/mm<sup>2</sup> or  $5.8 \pm 0.4$  nA/cm<sup>2</sup>.

After determining the beam profile of the incoming ion beam, sputtering yield measurements with the QCM could be conducted. As already mentioned on page 40, each measurement consisted of at least three phases. In phase one and three, the ion beam is blocked by the UHV shutter and the frequency drift (without irradiation), due to thermal instabilities, is monitored. The quartz crystal was only irradiated in phase two. This allowed us, on the one hand, to subtract the thermal frequency drift of the crystal from the frequency slope, which is used for the evaluation of the sputtering yield (cf.



4 Results and discussion

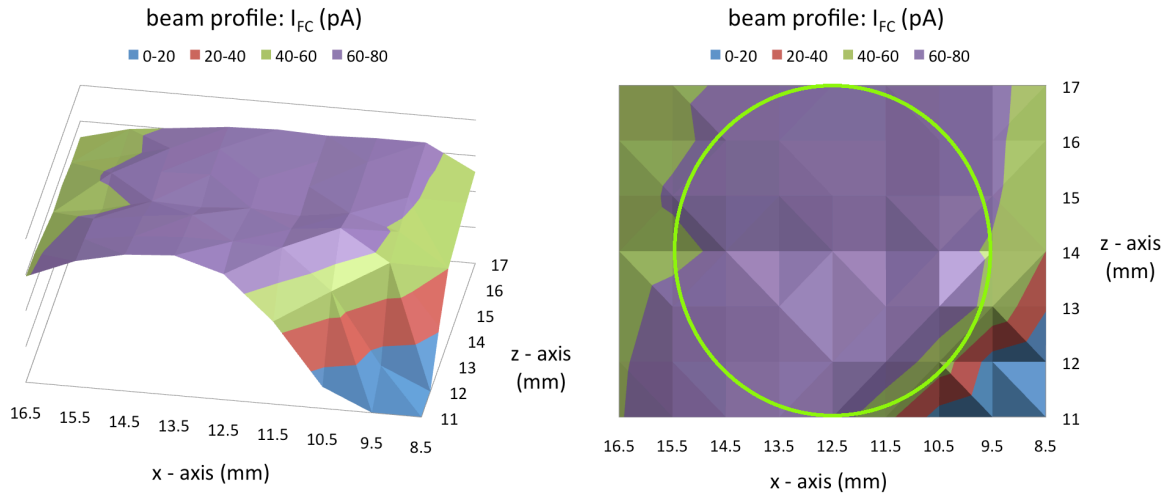


Figure 4.1: Typical beam profile of the ion beam obtained by scanning the ion beam. By increasing the voltage applied to the scanning plates, the beam spot size exceeds the size of the active area of the crystal (symbolized with the green circle with diameter of 6 mm). In this way the ion current impinging on the crystal is defined by the ion current density.

equation 3.3). On the other hand we were able to check the drift before and after each ion irradiation and to reject measurements, which exhibited to high drift changes, if necessary. In figure 4.2 two typical sputtering yield measurements of W by the bombardment of  $Ar^+$  are shown. To estimate the statistic measuring accuracy of our QCM setup, a series of such measurements under the same conditions was performed. By calculating the average and the corresponding standard deviation of the obtained sputtering yields, the statistic measuring error of the QCM setup was estimated to be less than 10% (at least for the investigated energies with this target-projectile combination).

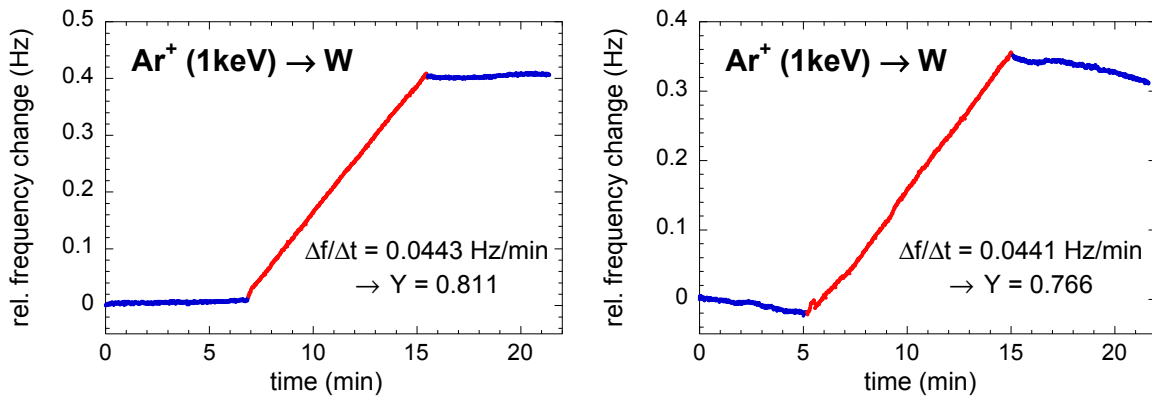


Figure 4.2: Typical QCM measurements of  $Ar^+$  ions with an impact energy of 1 keV

## 4.2 Cleaning of the target surface

(parts of this section will appear in [21])

Prior to N bombardment the tungsten surfaces were sputter cleaned in situ with  $\text{Ar}^+$  ions. Ar was chosen because it is a noble gas and is therefore not bond within the tungsten surface. Some  $10^{14}$   $\text{Ar}^+$  ions/ $\text{cm}^2$  were applied to the surface and the resulting sputtering yield was monitored. The development of the measured sputtering yield of W versus the incoming fluence of  $\text{Ar}^+$  ions is shown in figure 4.3. At first an elevated sputtering yield most likely resulting from an adsorbate, oxide or carbide layer on the tungsten surface was observed.  $\text{Ar}^+$  bombardment was continued until a steady state sputtering yield was reached.

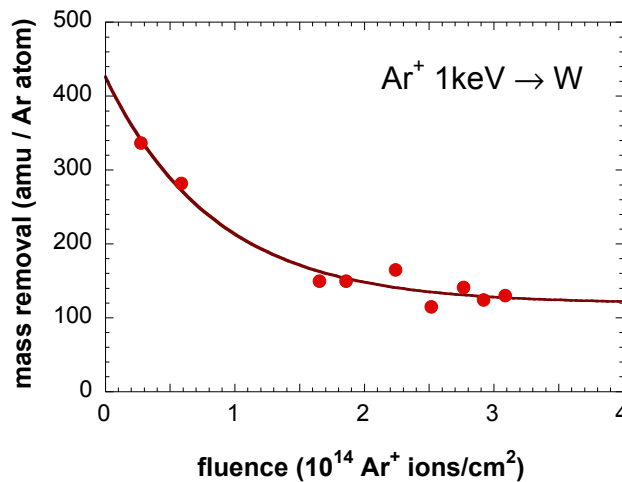


Figure 4.3: Before the measurements with  $\text{N}^+$  ions were started the W surface was sputter cleaned in situ with  $\text{Ar}^+$  ions. In the beginning, an increased sputtering yield is observed resulting most likely from an oxide or carbide layer on the tungsten surface.

Ion implantation in the target can lead to composition changes and can also effect the sputtering yield. Dynamic simulation programs such as TRIDYN can handle this implementation and can be used to estimate the accumulation of ions within the target surface. From a series of such TRIDYN simulations, one can expect that less than 10% Ar accumulates within the ion penetration depth after a fluence of  $10^{15}$  ions/ $\text{cm}^2$ . This is consistent with the expectations, since Ar is a noble gas and is therefore not bond within the tungsten surface. Therefore, for all further measurements with N, the W surface could be assumed to be a clean tungsten surface.

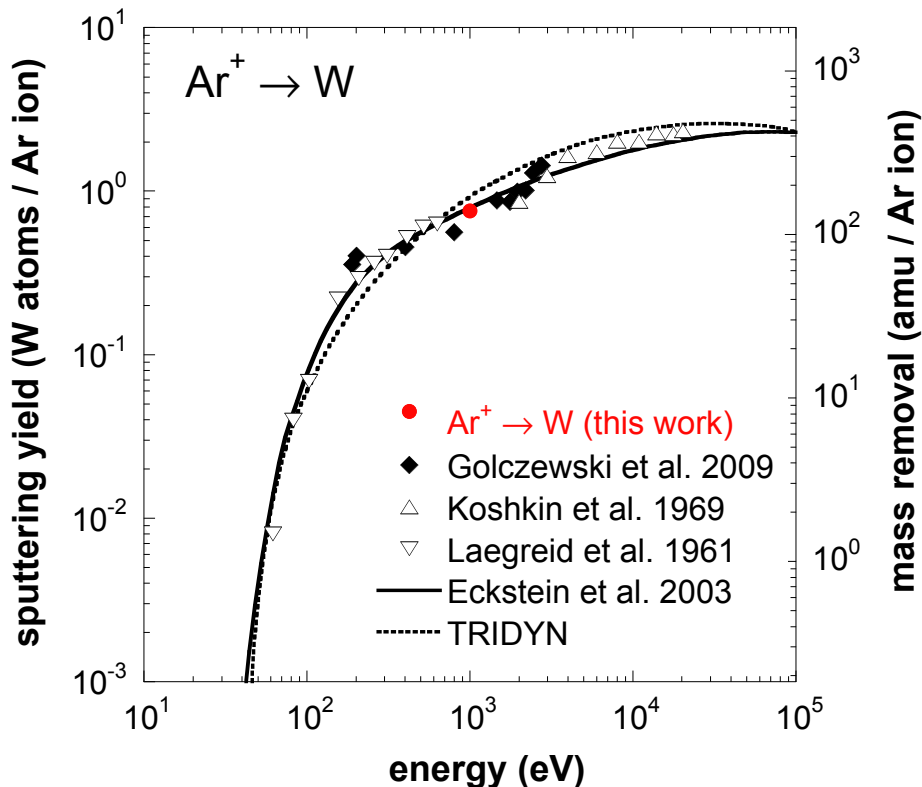


Figure 4.4: Sputtering yield of polycrystalline tungsten bombarded by  $\text{Ar}^+$  ions (full circles) vs. projectile energy. Previously published experimental data are included for comparison:  $\diamond$  [63]  $\triangle$  [73],  $\nabla$  [74]. The experimental data points are fitted with a function published by Eckstein and Preuss [55] with fitting parameters taken from [27]. Also shown are the TRIDYN [32] results of figure 2.1

With a sputtering yield of about 0.7 W atoms per  $\text{Ar}^+$  projectile of 1 keV (cf. figure 4.4 and Golczewski et al [63]) this corresponds to the removal of a few monolayers of tungsten only. The cleaning of the W surface by  $\text{Ar}^+$  ions gave us the possibility to compare our results of the sputtering yield of W by  $\text{Ar}^+$  ions with previous measured data since this projectile-target combination is already well known in the literature with both data from experiments and as well as from simulations. Figure 4.4 shows the sputtering yield of polycrystalline W with  $\text{Ar}^+$  in the energy range from 10 eV to 100 keV. Our measured data compare well with results from data from the literature (Golczewski et al [63], Koshkin et al [73] and Laegreid et al [74]). All data points are fitted by a formulae developed by Eckstein and Preuss [55] with fitting parameters taken from [27] and also compared to TRIDYN [32] calculations.

The cleaning procedure was then repeated with  $N^+$  ions with a kinetic energy of 1 keV, where again typically  $10^{15}$   $N^+$  ions/cm<sup>2</sup> were necessary to reach a steady state value. Figure 4.5 shows the levelling of the sputtering yield of W by the bombardment of  $N^+$  ions.

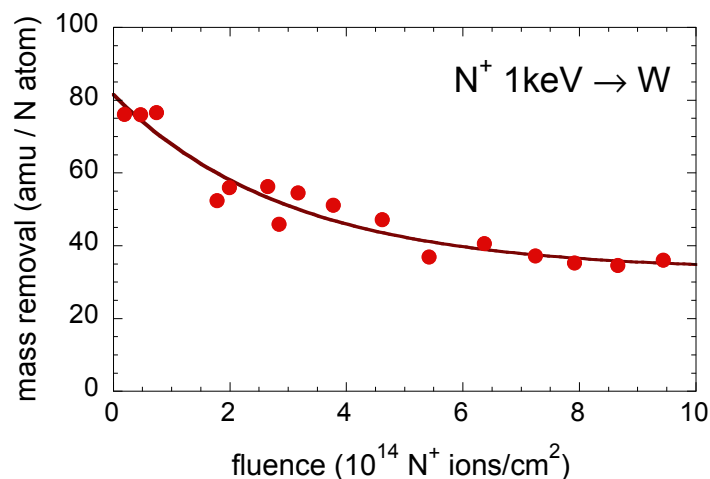


Figure 4.5: After the Ar bombardment we repeated the cleaning procedure with  $N^+$  ions. Some  $10^{15}$   $N^+$  ions/cm<sup>2</sup> were again necessary to reach a steady state value.

### 4.3 Sputtering of W by $N_2^+$ and $N^+$

(parts of this section will appear in [21])

Figure 4.6 shows measured sputtering yields of polycrystalline tungsten for both impact of molecular  $N_2^+$  and atomic  $N^+$  ions. For comparability the projectile energy as well as the sputtering yield are normalized to the number of N atoms in the projectile. In this way projectiles of equal velocity are compared and possible 'molecular effects' should become visible. To avoid systematic errors as much as possible, the results shown in figure 4.6 for  $N^+$  and  $N_2^+$  projectiles have been obtained in random order on different days and sometimes even different quartz crystals. Every data point shown is the result of at least 5 individual measurements usually carried out the same day on the same quartz crystal. In some but not all cases the measurements have been repeated on a different day, sometimes even on several different days and also on a different quartz crystal. The error bars shown correspond to the standard deviation of the mean value

of all the individual measurements. For this is the reason, some of the data points carry much smaller statistical error bars than others.

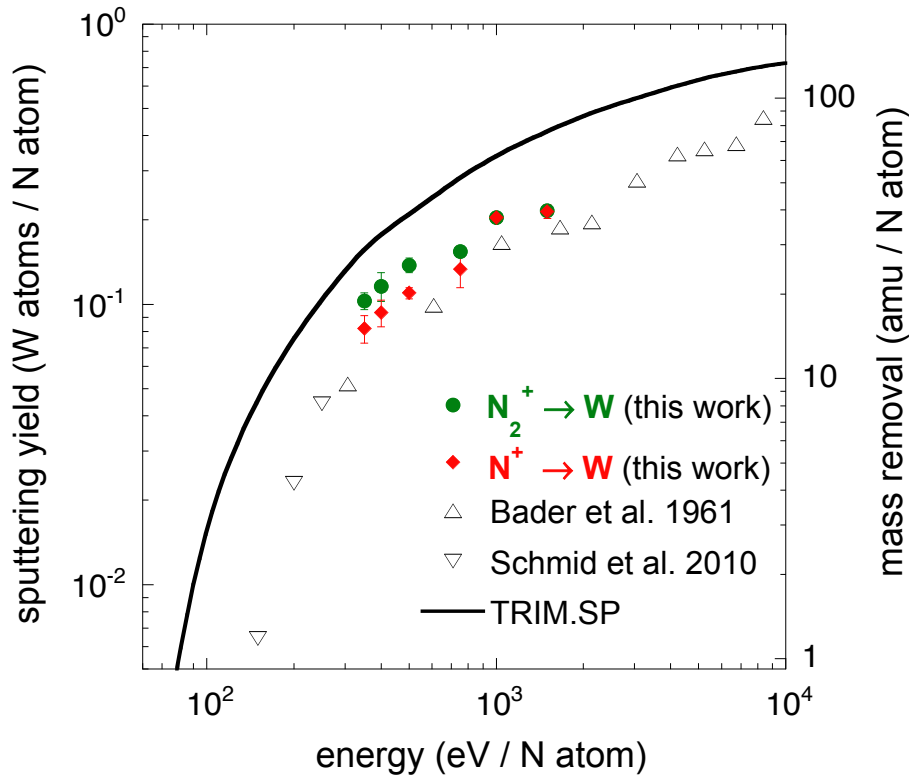


Figure 4.6: Sputtering yield per nitrogen atom of polycrystalline tungsten bombarded by molecular  $N_2^+$  ions (full circles) and by atomic  $N^+$  ions (full diamonds) vs. projectile energy per nitrogen atom. Previously published experimental data are included for comparison:  $\triangle$  [26],  $\nabla$  [28]

In figure 4.6 we also compare our data to the results of previous measurements by Schmid et al [28] and Bader et al [26] as well as a TRIM.SP [27] simulation. The TRIM.SP data are noticeably higher than all experimental data points and correspond to the 'static' TRIDYN [32] calculations presented by Schmid et al [28]. To explain the difference between their experimental data and those of the 'static' TRIDYN calculations, Schmid et al [28] argued that during the bombardment of W with high fluences of  $N^+$  ions, the accumulation of N in the surface leads to a tungsten-nitride phase within the ion implantation depth, thus reducing the sputtering yield as compared to a pure W surfaces. They obtained their data points by the bombardment with ions from a N plasma (composed of 90%  $N_2^+$  and 10%  $N^+$ ) with a fluence of some  $10^{19}$  ions/cm<sup>2</sup>, after which they found that the implantation of nitrogen in the surface layer had saturated.

The amount of N retained in W due to ion implantation depends on the implantation depth, the solubility of N in W, the rate which N diffuses into the W bulk and out of the sample [28] and of course on the fluence. The low diffusion of N in W for low temperatures leads to a quick saturation of N within the implantation zone at higher fluences. The solubility of N in W is determined by the thermodynamic phase in which the implanted N is retained. The maximum of the implanted N is given by the phase with the highest N content, which is at low temperatures according to Schmid et al [28] the WN phase. Therefore all N not bound in a nitride phase sublimates from the surface resulting in a maximum N surface concentration of 50% [28].

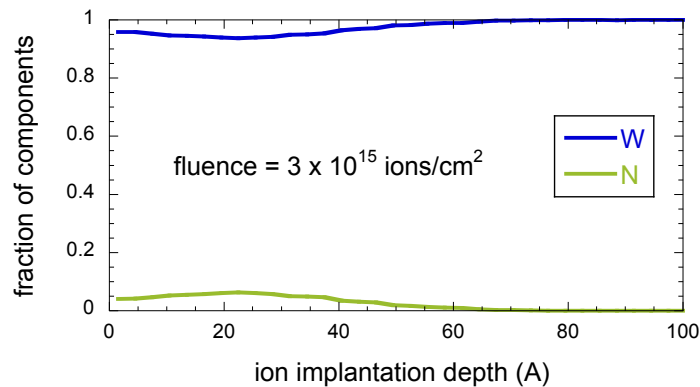


Figure 4.7: TRIDYN simulation showing the resulting fractions of the two components N and W after a fluence of  $3 \cdot 10^{15}$  ions/cm<sup>2</sup> for N<sup>+</sup> ions with an energy of 1 keV impinging onto the W surface.

In order to estimate the effect of nitrogen implantation on our sputtering results, we also performed dynamic TRIDYN simulations (cf. section Simulation on page 24). One of the key parameter for sputter calculations with TRIDYN or similar programs is the surface binding energy. In all these simulations the surface binding energy of nitrogen was kept constant at the value of pure W of 8.68 eV as it was also done by Schmid et al [28]. By setting the maximum fraction of N in the tungsten surface to 50% we allowed the formation of a WN layer. The results of the TRIDYN simulations can be seen in figure 4.7. As all our measurements are taken within a fluence of up to  $3 \cdot 10^{15}$  N<sup>+</sup> ions/cm<sup>2</sup> we also stopped our simulation at this fluence and looked at the amount of nitrogen within the ion implantation depth. As one can see from figure 4.7 the fraction of N within the implantation depth is less than 10%. This results in only a small reduction of the sputtering yield (within the experimental error of 10 %). Our results

#### 4 Results and discussion

given in figure 4.6 should therefore be representative for the case of a pure tungsten surface.

Further simulations have been performed to determine the fluence which is necessary to form a saturated tungsten-nitride layer within the implantation depth. Results of these simulations are given in figure 4.8. With increasing fluence, the N content within the W surface rises and saturates at a fluences above  $7.5 \cdot 10^{16} \text{ N}^+$  ions/cm<sup>2</sup>. After that, the depth profile of N and W does not change anymore with increasing fluence, although the target thickness still decreases.

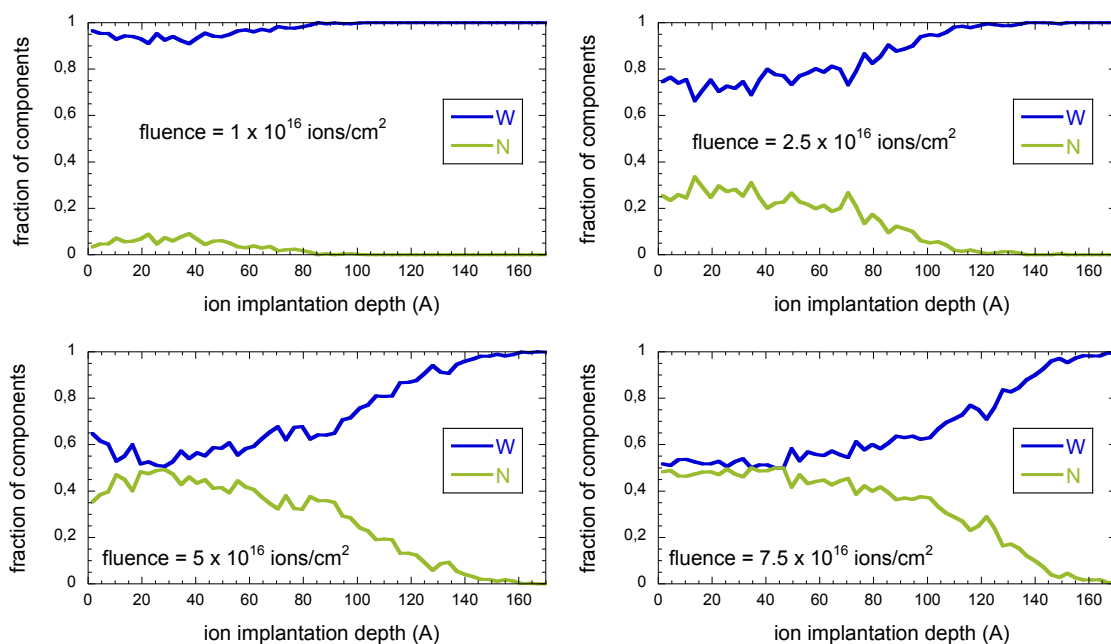


Figure 4.8: TRIDYN simulation showing the fractions of the two components N and W after various fluences of  $\text{N}^+$  ions with energy of 1 keV impinging onto the W surface. After a fluence of about  $7.5 \cdot 10^{16} \text{ ions/cm}^2$  the N accumulation has saturated.

## 4.4 Measured molecular effects

(parts of this section will appear in [21])

Taking a closer look at the differences between  $N^+$  and  $N_2^+$  sputtering yields in fig. 4.6 one finds that for energies above 1000 eV/N-atom the sputtering yields per N-atom nicely coincide for atomic and molecular ions. Below 1000 eV/N-atom, however, the amount of sputtered W atoms per incident N constituent in the projectile is clearly higher for the impact of a  $N_2^+$  molecular ion than for  $N^+$  atomic ion bombardment. In this energy range a  $N_2^+$  ion can thus obviously not be considered as equivalent to two separate N atoms impinging on the surface ('molecular effect'). This enhancement is clearly demonstrated in figure 4.9 by plotting the ratio between sputtering yields per atom for bombardment with molecular and atomic nitrogen ions for equally fast projectiles. At energies between 350 and 500 eV per nitrogen atom the sputtering yield per atom is about 25% higher for molecular than for atomic projectiles. Towards higher impact energies this enhancement diminishes and vanishes above 1000 eV/atom with the ratio of the two yields approaching one.

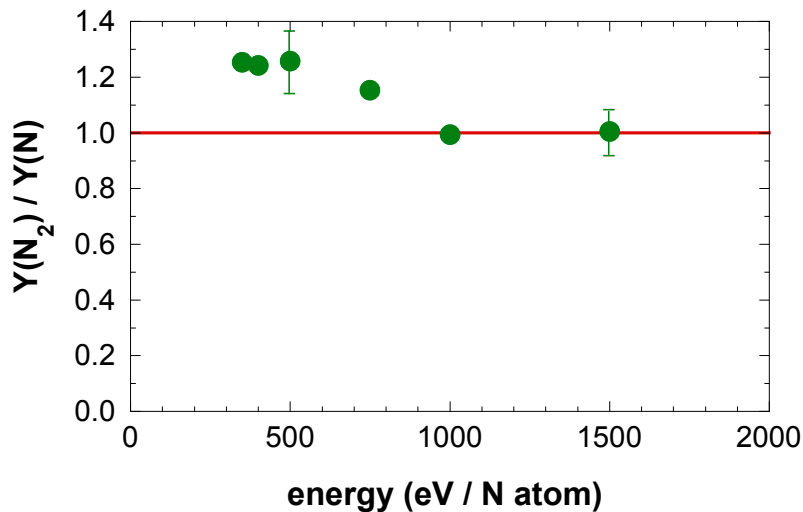


Figure 4.9: Ratio between sputtering yield per nitrogen atom for bombardment of tungsten with molecular as compared to equally fast atomic nitrogen ions (full symbols). The horizontal line corresponds to the linear case, where  $N_2^+$  acts as two independent atomic  $N^+$  projectiles.

At first glance such a pronounced molecular effect seems somewhat surprising. At high



energies (typically 50 keV or higher) molecular effects are well investigated and attributed to nonlinear effects in the collision cascade ([39, 40, 38]) as already mentioned in section 2.3. In the linear cascade regime of sputtering (typically 1 – 50 keV) the yield per atom of a molecular ion should equal that of an atomic ion at the same impact velocity (i.e. same energy per atomic constituent) [38]. Yao et al [41] were the first to show enhanced molecular sputtering yields compared to atomic sputtering yields in the near threshold region with projectile energies ranging from 50 to 500 eV.

For the qualitative explanation of the observed molecular effect, arguments, based on a simple energy transfer model, are given below. This model was first presented by Yao et al [41]. In their model the energy transferred to a target atom by a diatomic molecule is determined by an effective projectile mass  $m^*$  which varies between  $m \leq m^* \leq 2m$  depending on the relation between vibrational frequency of the molecule and collision time (and therefore projectile velocity). Two extreme cases are considered by Yao et al. In the limit of very large bond stiffness (high vibrational frequency/low impact energy) a  $N_2^+$  projectile can be treated as a single particle with twice the mass of a nitrogen atom, while in the limit of a weak bond (high impact energies) the two N atoms of the molecule act more or less independently.

In an elastic head-on collision the maximum energy transferable  $T_m$  for a projectile with mass  $m$  and kinetic energy  $E_0$  onto a target atom with mass  $M$  is given by equation 2.8 on page 19. In the case where projectile and target atom are equal in mass, the total kinetic energy of the projectile may be transferred in the collision, whereas, for a larger mismatch in the masses, only a fraction of the energy may be transferred. In the case of a  $^{14}N$  atom of energy  $E_0$  colliding with a  $^{184}W$  target the maximum energy transfer amounts to  $T_{atom} = 0.263 \cdot E_0$ . In the limiting case that the incident nitrogen molecule can be interpreted as a single rigid particle with a mass of 28 amu and a kinetic energy of  $2E_0$ , the energy transferred to a surface atom is increased to  $T_{molecule} = 0.459 \cdot 2E_0$  or  $0.459 \cdot E_0$  per incident nitrogen atom. From this simple estimate one finds that at very low impact energies, up to 1.7 times more energy per atom can be transferred to a W surface atom by a molecular nitrogen projectile than for atomic nitrogen bombardment. For collision times shorter than the vibrational period of the  $N_2$  molecule, i.e. for higher kinetic energies, the molecule will behave more like two single atoms and the energy transferred per incident N atom will become equal.

## 5 Summary and outlook

### Summary

Within the scope of this diploma thesis sputtering measurements for nitrogen bombardment of tungsten have been performed by using a quartz crystal microbalance setup previously developed at the TU Wien [61]. The interest in this projectile-target combination comes from its relevance for plasma-wall-interaction in thermonuclear fusion experiments. The tungsten target layer, deposited onto the beam-facing side of the quartz crystal, was bombarded by nitrogen ions. By using not only atomic  $N^+$  but also molecular  $N_2^+$  ions as projectiles, an unexpected non-linear effect was found. In general, it is often assumed that the impact of an  $X_n^+$  ion on a solid has the same effect as  $n \cdot X^+$  ions at the same velocity, especially in the low energy regime. By comparing the total sputtering yield per nitrogen atom of the two ion species at equal impact velocities, enhanced molecular sputtering yields have been found. This co-called 'molecular effect' was investigated in detail for several impact energies. It was concluded that it only exists in the near threshold region. At impact energies below 500 eV the sputtering yield per nitrogen atom for  $N_2^+$  molecular ions was found to be up to 25% higher than that of a single  $N^+$  ion with the same impact velocity. A qualitative explanation for this enhanced molecular sputtering yields could be given, based on a simple energy transfer model according to Yao et al [41]. The experimental results of the thesis have meanwhile been accepted for publication [21].

The nitrogen ions used for the experiments were generated in an ECR ion source located at the Institute of Applied Physics at TU Wien. During the conduction of this diploma thesis the vacuum system of the whole ion source facility had to be renewed which took considerable time. This included also the QCM beamline, which is one of the three beamlines connected to the ion source. Due to the change of the vacuum pumps

at the beamlines from turbo-molecular pumps to ion pumps, it was also necessary to design and build new support systems for the three beamlines. For this reason the three beamlines and the new support structure were modelled with the 3D modelling program SolidWorks. The other components of the facility, like the ion source or the magnets with their support structures, were subsequently added to the model bit by bit. The now, complete model of the whole facility allows to easily extract technical drawings of each component if needed and to illustrate the setup in an improved and presentable way. Furthermore the new design of the beamline support now facilitates maintenance work and the realization of changes to the vacuum components.

Not only the vacuum pumps of the beamlines were renewed, but also the vacuum pumps of the ion source and the magnets, the prevacuum pumps, pressure gauges, shutters, valves, manipulators and the complete wiring of these components. As also the target chamber and the manipulator of the QCM beamline changed, it was necessary to redesign the sample holder of the quartz crystal. The new design of the sample holder allows to change a crystal without having to remove the manipulator, as it was the case prior to the reconstruction.

## Outlook

Schmid et al [28] have studied the sputter erosion of W by high fluxes of  $N_2^+$  projectiles by irradiating W samples in a nitrogen plasma. After irradiation they observed the formation of a tungsten-nitride surface layer within the ion penetration depth with a N concentration of up to 50%. As a result the partial sputtering yield of tungsten is reduced, compared to a pure tungsten surface, due to preferential sputtering of nitrogen. By using a QCM such a measurement could be performed in situ and in real-time, which would allow to monitor transient effects in the sputtering yield with increasing fluence. In this way the required fluence to built up this tungsten-nitride layer could be determined. With our ion source sputter yield measurements up to a fluence of several  $10^{16}$  ions/cm<sup>2</sup> are certainly conceivable and a measuring campaign like this could be conducted within a few weeks.

Additionally, after preparing this WN-layer, eventually molecular-effects in the interac-

*5 Summary and outlook*

---

tion of this WN layer with  $N_2^+$  could be investigated by again comparing sputtering yields per nitrogen atoms of molecular ions with atomic ions.

Another measuring campaign is planned in cooperation with Priv. Doz. Dr. Christian Linsmeier at the IPP Garching aiming to determine the total sputtering yield of beryllium a material also relevant for plasma-wall-interaction. For this reason the whole QCM will be transferred from the ion source facility in Vienna to IPP Garching in the near future.

## Bibliography

- [1] Clery D., ‘ITER’s \$12 billion gamble’, *Science*, **314**, 238 (2006)
- [2] Nehring R., ‘Traversing the mountaintop: world fossil fuel production to 2050’, *Philosophical Transactions of the Royal Society B: Biological Sciences*, **364**, 3067 (2009)
- [3] Toschi R., ‘Nuclear fusion, an energy source’, *Fusion engineering and design*, **36**, 1 (1997)
- [4] Westra M.T., ‘Energy, Powering Your World’, EFDA, FOM - Institute for Plasma Physics Rijnhuizen, [http://www.efda.org/multimedia/booklets\\_and\\_articles.htm](http://www.efda.org/multimedia/booklets_and_articles.htm) (2005)
- [5] Dauer L.T., Zanzonico P., Tuttle R.M., Quinn D.M. and Strauss H.W., ‘The Japanese Tsunami and Resulting Nuclear Emergency at the Fukushima Daiichi Power Facility: Technical, Radiologic, and Response Perspectives’, *Journal of Nuclear Medicine*, **52**, 1423 (2011)
- [6] European Fusion Development Agreement (EFDA), ‘Advantages of fusion energy’, [http://www.efda.org/fusion\\_energy/advantages\\_of\\_fusion\\_energy.htm](http://www.efda.org/fusion_energy/advantages_of_fusion_energy.htm) (2011)
- [7] European Fusion Development Agreement (EFDA), ‘Picture gallery’, [http://www.efda.org/multimedia/picture\\_gallery.php](http://www.efda.org/multimedia/picture_gallery.php) (2011)
- [8] European Fusion Development Agreement (EFDA), ‘The current status of fusion research’, [http://www.efda.org/fusion\\_energy/fusion\\_research\\_today.htm](http://www.efda.org/fusion_energy/fusion_research_today.htm) (2011)
- [9] ITER, ‘milestones’, <http://www.iter.org/proj/itermilestones> (2011)
- [10] European Fusion Development Agreement (EFDA), ‘The ITER project’, [http://www.efda.org/the\\_iter\\_project/introduction\\_to\\_iter.htm](http://www.efda.org/the_iter_project/introduction_to_iter.htm) (2011)
- [11] Lawson J.D., ‘Some criteria for a power producing thermonuclear reactor’, *Proceedings of the Physical Society. Section B*, **70**, 6 (1957)

- [12] JET, ‘Conditions for a fusion reaction’,  
<http://www.jet.efda.org/fusion-basics/conditions-for-a-fusion-reaction/> (2011)
- [13] Wikipedia, ‘Fusion reaction rate’,  
[http://en.wikipedia.org/wiki/File:Fusion\\_rxnrate.svg](http://en.wikipedia.org/wiki/File:Fusion_rxnrate.svg) (2011)
- [14] Boozer A.H., ‘Physics of magnetically confined plasmas’, *Reviews of Modern Physics*, **76**, 1071 (2005)
- [15] European Fusion Development Agreement (EFDA), ‘Introduction to fusion’,  
[http://www.efda.org/fusion\\_energy/introduction\\_to\\_fusion.htm](http://www.efda.org/fusion_energy/introduction_to_fusion.htm) (2011)
- [16] Pitcher C.S. and Stangeby P., ‘Experimental divertor physics’, *Plasma Physics and Controlled Fusion*, **39**, 779 (1997)
- [17] Federici G., Skinner C.H., Brooks J.N., Coad J.P., Grisolia C., Haasz A.A., Hasanein A., Philipps V., Pitcher C.S., Roth J., Wampler W.R. and Whyte D.G., ‘Plasma-material interactions in current tokamaks and their implications for next step fusion reactors’, *Nuclear Fusion*, **41**, 1967 (2001)
- [18] Parker R., Janeschitz G., Pacher H., Post D., Chiocchio S., Federici G. and Ladd P., ‘Plasma-wall interactions in ITER’, *Journal of Nuclear Materials*, **241-243**, 1 (1997)
- [19] Federici G., Andrew P., Barabaschi P., Brooks J., Doerner R., Geier A., Herrmann A., Janeschitz G., Krieger K., Kukushkin A., Loarte A., Neu R., Saibene G., Shimada M., Strohmayer G. and Sugihara M., ‘Key ITER plasma edge and plasma-material interaction issues’, *Journal of Nuclear Materials*, **313-316**, 11 (2003)
- [20] Barabash V., Akiba M., Cardella A., Mazul I., Odegard B.C., Plöchl L., Tivey R. and Vieider G., ‘Armor and heat sink materials joining technologies development for ITER plasma facing components’, *Journal of Nuclear Materials*, **283-287**, 1248 (2000)
- [21] Dobes K., Naderer P., Eisenmenger-Sittner C. and Aumayr F., ‘Sputtering of tungsten by  $N^+$  and  $N_2^+$  ions – investigations of molecular effects’, *Physica Scripta* (2011), in print
- [22] Kallenbach A., Balden M., Dux R., Eich T., Giroud C., Huber A., Maddison G.P., Mayer M., McCormick K. and Neu R., ‘Plasma surface interactions in impurity seeded plasmas’, *Journal of Nuclear Materials* (2011), in print
- [23] Kallenbach A., Dux R., Mayer M., Neu R., Pütterich T., Bobkov V., Fuchs J.C., Eich T., Giannone L., Gruber O., Herrmann A., Horton L.D., Maggi C.F., Meister

- H., Müller H.W., Rohde V., Sips A., Stähler A., Stober J. and the ASDEX Upgrade Team, 'Non-boronized compared with boronized operation of ASDEX Upgrade with full-tungsten plasma facing components', *Nuclear Fusion*, **49**, 045007 (2009)
- [24] Maddison G., McCormick K., Giroud C., Alonso A., Alper B., Andrew Y., Arnoux G., Belo P., Beurskens M., Boboc A., Brezinsek S., Brix M., Coffey I., de la Luna E., de Vries P., Devaux S., Eich T., Felton R., Fundamenski W., Harting D., Hobirk J., Huber A., Jachmich S., Jenkins I., Joffrin E., Kallenbach A., Kempenaars M., Lehnen M., Loarer T., Lomas P., McDonald D., Meigs A., Morgan P., Ongena J., Riccardo V., Rimini F., Sirinelli A., Stamp M., Telesca G., Thomsen H. and JET EFDA contributors, 'Impurity-seeding experiments on JET in preparation for the ITER-like wall', *Proceedings of 36th EPS Conference on Controlled Fusion and Plasma Physics, Sofia, Bulgaria, European Physical Society*, **33**, 2160 (2009)
- [25] Kallenbach A., Dux R., Fuchs J.C., Fischer R., Geiger B., Giannone L., Herrmann A., Lunt T., Mertens V., McDermott R., Neu R., Pütterich T., Rathgeber S., Rohde V., Schmid K., Schweinzer J., Treutterer W. and the ASDEX Upgrade Team, 'Divertor power load feedback with nitrogen seeding in ASDEX Upgrade', *Plasma Physics and Controlled Fusion*, **52**, 055002 (2010)
- [26] Bader M., Witteborn F. and Snouse T., 'Sputtering of metals by mass-analyzed  $N_2^+$  and  $N^+$ ', Technical report, National Aeronautics and Space Administration. Ames Research Center, California (1961)
- [27] Behrisch R. and Eckstein W., *Sputtering by Particle Bombardment III: Experiments and Computer Calculations from Threshold to MeV Energies*, Springer Berlin (2007)
- [28] Schmid K., Manhard A., Linsmeier C., Wiltner A., Schwarz-Selinger T., Jacob W. and Mändl S., 'Interaction of nitrogen plasmas with tungsten', *Nuclear Fusion*, **50**, 025006 (2010)
- [29] Andersen H.H., Bay H.L., Behrisch R., Robinson M.T., Roosendaal H.E. and Sigmund P., *Sputtering by Particle Bombardment*, Springer Berlin (1981)
- [30] Aumayr F. and Winter HP., 'Potential sputtering', *Philosophical Transactions of the Royal Society of London. Series A: Mathematical, Physical and Engineering Sciences*, **362**, 77 (2004)
- [31] Winters H. and Coburn J., 'Surface science aspects of etching reactions', *Surface Science Reports*, **14**, 162 (1992)
- [32] Möller W. and Eckstein W., 'TRIDYN - A TRIM simulation code including dynamic composition changes', *Nuclear Instruments and Methods in Physics Research B*, **2**, 814 (1984)

- [33] Eckstein W., *Computer Simulation of Ion Solid Interaction*, volume 10 of *Material Science*, Springer, Berlin, Heidelberg (1991)
- [34] Weissmann R. and Sigmund P., ‘Sputtering and backscattering of keV light ions bombarding random targets’, *Radiation Effects*, **19**, 7 (1973)
- [35] Sigmund P., ‘Theory of sputtering. I. Sputtering yield of amorphous and polycrystalline targets’, *Physical Review*, **184**, 383 (1969)
- [36] Nastasi M.A., Mayer J.W. and Hirvonen J.K., *Ion-solid interactions: fundamentals and applications*, Cambridge University Press (1996)
- [37] Ziegler J.F., ‘SRIM The Stopping and Range of Ions in Matter’, available from: <http://www.srim.org/> (2008)
- [38] Andersen H.H., ‘Fundamental Processes in Sputtering of Atoms and Molecules’, *Royal Danish Academy of Science and Letters*, **92**, 127 (1993)
- [39] Andersen H.H. and Bay H.L., ‘Nonlinear effects in heavy-ion sputtering’, *Journal of Applied Physics*, **45**, 953 (1974)
- [40] Andersen H.H. and Bay H.L., ‘Heavy-ion sputtering yields of gold: Further evidence of nonlinear effects’, *Journal of Applied Physics*, **46**, 2416 (1975)
- [41] Yao Y., Hargitai Z., Albert M., Albridge R., Barnes A., Gilligan J., Pratt Ferguson B., Lüpke G., Gordon V., Tolk N., Tully J., Betz G. and Husinsky W., ‘New molecular collisional interaction effect in low-energy sputtering’, *Physical Review Letters*, **81**, 550 (1998)
- [42] Meyer F.W., Zhang H., Lance M. and Krause H., ‘Chemical sputtering and surface damage of graphite by low-energy atomic and molecular hydrogen and deuterium projectiles’, *Vacuum*, **82**, 880 (2008)
- [43] Harris P.R., Meyer F.W., Jacob W., Schwarz-Selinger T. and von Toussaint U., ‘Molecular size effect in the chemical sputtering of a-C:H thin films by low energy  $H^+$ ,  $H_2^+$ , and ions  $H_3^+$ ’, *Nuclear Instruments and Methods in Physics Research Section B: Beam Interactions with Materials and Atoms*, **269**, 1276 (2011)
- [44] Behrisch R., *Sputtering by Particle Bombardment II: Sputtering of Alloys and Compounds, Electron and Neutron Sputtering, Surface Topography*, Springer Berlin (1983)
- [45] Arnau A., Aumayr F., Echenique P., Grether M., Heiland W., Limburg J., Morgen-



- stern R., Roncin P., Schippers S. and Schuch R., 'Interaction of slow multicharged ions with solid surfaces', *Surface Science Reports*, **27**, 113 (1997)
- [46] Schenkel T., Hamza A.V., Barnes A.V. and Schneider D.H., 'Interaction of slow, very highly charged ions with surfaces', *Progress in Surface Science*, **61**, 23 (1999)
- [47] Winter HP. and Aumayr F., 'Hollow atoms', *Journal of Physics B: Atomic, Molecular and Optical Physics*, **32**, R39 (1999)
- [48] Winter HP. and Aumayr F., 'Slow multicharged ions hitting a solid surface: From hollow atoms to novel applications', *Europhysics News*, **33**, 3 (2002)
- [49] Aumayr F., Varga P. and Winter HP., 'Potential sputtering: desorption from insulator surfaces by impact of slow multicharged ions', *International Journal of Mass Spectrometry*, **192**, 415 (1999)
- [50] Neidhart T., Pichler F., Aumayr F., Winter HP., Schmid M. and Varga P., 'Potential Sputtering of Lithium Fluoride by Slow Multicharged Ions', *Physical Review Letters*, **74**, 5280 (1995)
- [51] Sporn M., Libiseller G., Neidhart T., Schmid M., Aumayr F., Winter HP., Varga P., Grether M., Niemann D. and Stolterfoht N., 'Potential Sputtering of Clean SiO<sub>2</sub> by Slow Highly Charged Ions', *Physical Review Letters*, **79**, 945 (1997)
- [52] Roth J., 'Chemical erosion of carbon based materials in fusion devices', *Journal of Nuclear Materials*, **266-269**, 51 (1999)
- [53] Biersack J.P. and Haggmark L.G., 'A Monte Carlo computer program for the transport of energetic ions in amorphous targets', *Nuclear Instruments and Methods*, **174**, 257 (1980)
- [54] Biersack J.P. and Eckstein W., 'Sputtering studies with the Monte Carlo Program TRIM.SP', *Applied Physics A: Materials Science & Processing*, **34**, 73 (1984)
- [55] Eckstein W. and Preuss R., 'New fit formulae for the sputtering yield', *Journal of Nuclear Materials*, **320**, 209 (2003)
- [56] Möller W., Eckstein W. and Biersack J., 'TRIDYN - binary collision simulation of atomic collisions and dynamic composition changes in solids', *Computer Physics Communications*, **51**, 355 (1988)
- [57] Bohdansky J., 'A universal relation for the sputtering yield of monatomic solids at normal ion incidence', *Nuclear Instruments and Methods in Physics Research Section B: Beam Interactions with Materials and Atoms*, **2**, 587 (1984)

- [58] Wilson W.D., Haggmark L. and Biersack J.P., ‘Calculations of nuclear stopping, ranges, and straggling in the low-energy region’, *Physical Review B*, **15**, 2458 (1977)
- [59] Sauerbrey G., ‘Use of quartz vibrator for weighing thin layers and as a microbalance’, *Zeitschrift für Physik*, **155**, 206 (1959)
- [60] Neidhart T., Toth Z., Hochhold M., Schmid M. and Varga P., ‘Total sputter yield of LiF induced by hyperthermal ions measured by a quartz microbalance’, *Nuclear Instruments and Methods in Physics Research Section B: Beam Interactions with Materials and Atoms*, **90**, 496 (1994)
- [61] Hayderer G., Schmid M., Varga P., Winter HP. and Aumayr F., ‘A highly sensitive quartz-crystal microbalance for sputtering investigations in slow ion–surface collisions’, *Review of Scientific Instruments*, **70**, 3696 (1999)
- [62] Golczewski A., Dobes K., Wachter G., Schmid M. and Aumayr F., ‘A quartz-crystal-microbalance technique to investigate ion-induced erosion of fusion relevant surfaces’, *Nuclear Instruments and Methods in Physics Research Section B: Beam Interactions with Materials and Atoms*, **267**, 695 (2009)
- [63] Golczewski A., Kuzucan A., Schmid K., Roth J., Schmid M. and Aumayr F., ‘Ion-induced erosion of tungsten surfaces studied by a sensitive quartz-crystal-microbalance technique’, *Journal of Nuclear Materials*, **390**, 1102 (2009)
- [64] Hayderer G., ‘Projectile charge state dependent sputtering of solid surfaces’, Ph.D. thesis, TU Wien (2000)
- [65] Galutschek E., ‘Development of a 14.5 GHz All-Permanent Magnet Multicharged ECR Ion Source for Remote Operation’, Ph.D. thesis, TU Wien (2005)
- [66] Galutschek E., Trassl R., Salzborn E., Aumayr F. and Winter HP., ‘Compact 14.5 GHz all-permanent magnet ECRIS for experiments with slow multicharged ions’, *Journal of Physics: Conference Series*, **58**, 395 (2007)
- [67] Mironov V., Stiebing K., Hohn O., Schmidt L., Schmidt-Böcking H., Runkel S., Schempp A., Shirkov G., Biri S. and Kenéz L., ‘Influence of the biased electrode on the plasma potential in ECRIS’, *Review of Scientific Instruments*, **73**, 623 (2002)
- [68] Iskratsch K., ‘New Design of an Ion Source Control Software and Investigations of Ion-Induced Electron Emission from LiF’, Master’s thesis, TU Wien (2009)
- [69] Dobes K., ‘Erosion and Retention Investigations for Fusion Relevant Target-Projectile Combinations’, Master’s thesis, TU Wien (2009)

- 
- [70] Gamma Vacuum, 'Operation', <http://www.gammavacuum.com/operation.asp> (2011)
- [71] ITEM, 'MB Building Kit system', <http://www.item24.com> (2011)
- [72] Kowarik G., *Ausschreibungsunterlagen Vakuumanlage AUGUSTIN*, TU Wien (2010)
- [73] Koshkin V.K., Rysov J.A., I. I. Shkarban B.M. and Gourmin, 'On the cathode sputtering of polycrystals', in *Phenomena in Ionized Gases, Ninth International Conference*, volume 1, 92 (1969)
- [74] Laegreid N. and Wehner G.K., 'Sputtering yields of metals for Ar<sup>+</sup> and Ne<sup>+</sup> ions with energies from 50 to 600 eV', *Journal of Applied Physics*, **32**, 365 (1961)

# List of Figures

- 1.1 Schematic drawing of ITER: The woman at the bottom shows the scale of this machine (Picture taken from [7]) . . . . . 3
- 1.2 Reaction rate versus temperature: Compared with other fusion reactions, the D-T reaction has the highest reaction rate at the lowest temperature. (Picture taken from [13]) . . . . . 6
- 1.3 A schmeatic drawing of a tokamak with poloidal and toroidal coils and the resulting helical magnetic field lines (Picture taken from [15]) . . . . . 7
- 1.4 Sectional view of the ITER tokamak with sketched magnetic field lines: The separatix or last closed flux surface (LCFS) separates the plasma core from the scrape of layer (SOL) (Picture taken from [17]) . . . . . 9
- 1.5 ITER wall materials: The blanket modules will be made out of beryllium. For the divertor carbon in form of CFC and tungsten will be used (Picture taken from [9]) . . . . . 10
  
- 2.1 Typical dependence of the sputtering yield of tungsten due to the impact of either argon, neon, nitrogen or deuterium ions simulated with TRIDYN [32] in static mode. . . . . 15
- 2.2 Nuclear and electronic stopping power for argon and nitrogen ions in tungsten as cualculated using SRIM 2008 [37]. . . . . 19
- 2.3 Mean ion range of nitrogen ions in tungsten as cualculated using SRIM 2008 [37]. . . . . 22
  
- 3.1 Principle of the quartz crystal microbalance technique: The mass of the crystal defines the eigen-frequency of the thickness-shear-mode. This also holds true for a thin film of target material (W) deposited onto the crystal. Mass changes, due to the impact of incoming particles, are proportional to a frequency change, which can be measured with high accuracy. . . . . 27
- 3.2 Sample holder with the quartz crystal (colored in red), the heating (colored in yellow) and the tungsten spring (colored in blue) . . . . . 30
- 3.3 The QCM holder is now divided into two parts: the upper part, which is the connection to the UHV manipulator, remains in the vacuum chamber all the time, whereas the lower part (coloured in green) can be dismantled by simply loosening the red coloured screws on the top. All electrical connections, except the thermocouple, are now implemented using push connectors. This allows us to easily plug and unplug all wires within the vacuum chamber. . . . . 31

3.4	The frequency of a quartz crystal depending on the temperature shows a minimum usually in the range between 185°C and 200°C. In the case shown above, the minimum lies at about 190°C . . . . .	32
3.5	Butterworth - van Dyke circuit: This is the equivalent circuit of the quartz crystal. . . . .	33
3.6	Computer model of the ion source SOPHIE at TU Wien used to produce the ions for the sputtering yield measurements . . . . .	35
3.7	A sectional view of the ion source showing the microwave system, the plasma chamber surrounded by the permanent magnets and the extraction system. Picture taken from [65] . . . . .	36
3.8	Schematic overview of the experimental setup at the Institute of Applied Physics at TU Wien . . . . .	37
3.9	QCM block diagram . . . . .	38
3.10	Computer model of the lens system used to focus and decelerate the ions when needed. . . . .	39
3.11	Computer model of the whole ion source facility at the Institute of Applied Physics at TU Wien showing the ion source, the quadrupole magnet, the two sector magnets and the three beamlines. . . . .	43
3.12	Model of the vacuum system of one beamline showing the two ion pumps produced by Gamma Vacuum . . . . .	45
3.13	Plan of the vacuum system for one beamline. . . . .	46
3.14	Plan of the whole vacuum system taken from [72] . . . . .	48
4.1	Typical beam profile of the ion beam obtained by scanning the ion beam. By increasing the voltage applied to the scanning plates, the beam spot size exceeds the size of the active area of the crystal (symbolized with the green circle with diameter of 6 mm). In this way the ion current impinging on the crystal is defined by the ion current density. . . . .	50
4.2	Typical QCM measurements of Ar <sup>+</sup> ions with an impact energy of 1 keV	50
4.3	Before the measurements with N <sup>+</sup> ions were started the W surface was sputter cleaned in situ with Ar <sup>+</sup> ions. In the beginning, an increased sputtering yield is observed resulting most likely from an oxide or carbide layer on the tungsten surface. . . . .	51
4.4	Sputtering yield of polycrystalline tungsten bombarded by Ar <sup>+</sup> ions (full circles) vs. projectile energy. Previously published experimental data are included for comparison: $\diamond$ [63] $\triangle$ [73], $\nabla$ [74]. The experimental data points are fitted with a function published by Eckstein and Preuss [55] with fitting parameters taken from [27]. Also shown are the TRIDYN [32] results of figure 2.1 . . . . .	52
4.5	After the Ar bombardment we repeated the cleaning procedure with N <sup>+</sup> ions. Some 10 <sup>15</sup> N <sup>+</sup> ions/cm <sup>2</sup> were again necessary to reach a steady state value. . . . .	53

4.6	Sputtering yield per nitrogen atom of polycrystalline tungsten bombarded by molecular $N_2^+$ ions (full circles) and by atomic $N^+$ ions (full diamonds) vs. projectile energy per nitrogen atom. Previously published experimental data are included for comparison: $\triangle$ [26], $\nabla$ [28] . . . . .	54
4.7	TRIDYN simulation showing the resulting fractions of the two components N and W after a fluence of $3 \cdot 10^{15}$ ions/cm <sup>2</sup> for $N^+$ ions with an energy of 1 keV impinging onto the W surface. . . . .	55
4.8	TRIDYN simulation showing the fractions of the two components N and W after various fluences of $N^+$ ions with energy of 1 keV impinging onto the W surface. After a fluence of about $7.5 \cdot 10^{16}$ ions/cm <sup>2</sup> the N accumulation has saturated. . . . .	56
4.9	Ratio between sputtering yield per nitrogen atom for bombardment of tungsten with molecular as compared to equally fast atomic nitrogen ions (full symbols). The horizontal line corresponds to the linear case, where $N_2^+$ acts as two independent atomic $N^+$ projectiles. . . . .	57

## Danksagung

Bei den vielen Menschen, die zum Gelingen dieser Diplomarbeit beigetragen haben, möchte ich mich nun im folgenden bedanken.

Zu aller erst möchte ich Prof. Friedrich Aumayr, dem Betreuer meiner Diplomarbeit danken. Bereits in den ersten Studienjahren, in Grundlagen der Physik, hatte ich das Glück ihn kennen zu lernen. Seine Art, schwierige physikalische Problemstellungen auf einfache Weise zu erklären, wird mir immer ein Vorbild sein. Während der Durchführung dieser Diplomarbeit stand er mir immer mit hilfreichen Anregungen zur Seite und hat es mir darüber hinaus ermöglicht diverse Erfahrungen in der Welt der Wissenschaft zu sammeln. Vielen Dank Fritz.

Bedanken möchte ich mich zudem bei der gesamten Arbeitsgruppe für Atom- und Plasmaphysik für die freundliche und kollegiale Atmosphäre, zu der jeder einzelne von euch beigetragen hat. Besonders hervorheben möchte ich dabei DI Katharina Dobes für die äußerst kompetente Unterstützung beim Kennenlernen der Mikrowaage. Du hast mir auch geholfen, meine Angst vor spärlich gefüllten Datenbanken abzulegen. Durch die Erneuerung der Vakuumanlage im AUGUSTIN Labor durfte ich auch einige Zeit mit Dr. Gregor Kowarik zusammenarbeiten. Sein Wissen und seine Erfahrung im Labor waren mir stets eine große Hilfe. Unsere gemeinsamen Stunden beim Einziehen von Kabelsträngen werde ich immer mit einem Schmunzeln in Erinnerung behalten. Danken möchte auch B.Sc. Elisabeth Gruber, meiner Büro und Labor Kollegin, für die angenehme Zusammenarbeit während des Laborumbaus.

Vielen Dank möchte ich weiters B.Sc. Paul Berlinger, unseren Elektronikfachmann, aussprechen. Seine freundliche und kompetente Unterstützung und schnellen Reparaturen hielten das Experiment am Laufen. Ein großes Dankeschön ergeht weiters an die Mitarbeiter der Werkstätte: Wolfgang Beck, Herbert Schmidt und vor allem Rainer Gärtner, die mir nicht nur bei der Umgestaltung des Probenhalters sondern auch bei den unzähligen Umbauarbeiten im Labor tatkräftig zu Hilfe gestanden sind.

Nicht weniger wichtig für die Durchführung dieser Arbeit war auch die Unterstützung von meiner Familie und meinen Freunden. Bei meinen Eltern Berta und Franz möchte ich mich auf diesem Weg bedanken, dass sie mir dieses Studium ermöglicht haben. Eure Erziehung hat mich zu einem aufgeschlossenen und aufrichtigen Menschen gemacht. Einen herzlichen Dank auch an meine Brüder Thomas, Markus und Hannes und an

---

meine vielen lieben Freunden für die erfolgreiche Ablenkung und das Interesse an meinem Diplomarbeitsthema.

Zu guter Letzt möchte ich dir Olivia danken, für deine Liebe und dein Verständnis, nicht nur während des letzten Jahres. Du warst während der gesamten Zeit meines Studiums für mich da und hast mich auch in schwierigen Zeiten unterstützt. Besonders danken möchte ich dir für dein Verständnis im letzten Jahr, wenn es im Labor mal wieder etwas länger gedauert hat.